Title :

Oscillation-driven memory encoding, maintenance and recall in an entorhinal-hippocampal circuit model

Authors

Tomoki Kurikawa[1], Kenji Mizuseki[2], and Tomoki Fukai[3,4]

1. Department of Physics, Kansai Medical University, Hirakata, Osaka 573-1191, Japan
2. Department of Physiology, Osaka City University Graduate School of Medicine, Abeno-ku, Osaka, 545-8585, JAPAN
3. Okinawa Institute of Science and Technology, Onna-son, Okinawa 904-0495, Japan
4. RIKEN Center for Brain Science, Wako, Saitama 351-0198, Japan

Telephone: +81-72-804-2357

E-mail address: kurikawt@hirakata.kmu.ac.jp

A brief running title: Oscillation-driven memory encoding, maintenance and recall

Abstracts

During the execution of working memory tasks, task-relevant information is processed by local circuits across multiple brain regions. How this multi-area computation is conducted by the brain remains largely unknown. To explore such mechanisms in spatial working memory, we constructed a neural network model involving parvalbumin-positive, somatostatin-positive and vasoactive intestinal polypeptide-positive interneurons in the hippocampal CA1 and the superficial and deep layers of medial entorhinal cortex (MEC). Our model is based on a hypothesis that cholinergic modulations differently regulate information flows across CA1 and MEC at memory encoding, maintenance and recall during delayed nonmatching-to-place tasks. In the model, theta oscillation coordinates the proper timing of interactions between these regions. Furthermore, the model predicts that MEC is engaged in decoding as well as encoding spatial memory, which we confirmed by experimental data analysis. Thus, our model accounts for the neurobiological characteristics of the cross-area information routing underlying working memory tasks.

Keywords

cholinergic modulations, cross-area communications, disinhibitory circuit, spatial working memory

Introduction

Spatial navigation is a fundamental cognitive function that requires the processing of spatial memory by the hippocampus and entorhinal cortex. During a spatial navigation task, spatial information relevant to the task has to be encoded into, maintained in and recalled from spatial working memory at behaviorally adequate times. How these operations are coordinated by the cortico-hippocampal neural circuits during a spatial working memory task has yet to be explored.

A spatial working memory task is processed by several cortical areas such as the medial prefrontal cortex (mPFC) (Jones and Wilson 2005; Benchenane et al. 2010; Spellman et al. 2015), medial entorhinal cortex (MEC)(Suh et al. 2011; Yamamoto et al. 2014) and the hippocampal area CA1 (Benchenane et al. 2010). These anatomically connected areas (Swanson and Cowan 1977; Witter et al. 2000; Eichenbaum 2017) are thought to communicate mutually information necessary to accomplish the task. Importantly, the degree of functional importance of different inter-area connections varies during the task. This is indicated by the fact that the impairment of these connections at different behavioral phases differentially influences task performance (Suh et al. 2011; Yamamoto et al. 2014; Spellman et al. 2015). For instance, in a delayed nonmatching to place task (DNMP), the maintenance of spatial memory during a delay period does not require synaptic connections from the layer 3 of the MEC (MECIII) to CA1, but these connections are necessary for memory recall (Yamamoto et al. 2014). Connections from CA1 to the mPFC play a crucial role in memory encoding but not in memory recall (Spellman et al. 2015). These results indicate that information flows via the hippocampal circuit are not static but are dynamically regulated depending on the behavioral demands.

Dynamic information routing across multiple areas is thought to reflect in coherence in neuronal activity between different areas (Yamamoto et al. 2014; Spellman et al. 2015), which leads to the hypothesis called “communication through coherence”(Fries 2015). Many theoretical (Vogels and Abbott 2005; Akam and Kullmann 2010; Buehlmann and Deco 2010; Yang et al. 2016; Palmigiano et al. 2017) and experimental (Womelsdorf et al. 2014; Letzkus et al. 2015) studies have explored the gating functions for this dynamic processing. However, how the computations installed at multiple cortical areas are integrated to execute a spatial working memory task including different cognitive epochs (encoding, maintenance, and decoding) remains largely unclear.

Here, we elucidated the underlying mechanisms of multi-area dynamic information processing during DNMP tasks. We hypothesize that acetylcholine (ACh) controls spatial information flows in the entorhinal-hippocampal circuit according to different cognitive demands. Indeed, ACh is involved in diverse cognitive functions (Parikh et al. 2007; Hasselmo and Sarter 2010) including fear conditioning (Letzkus et al. 2011; Pi et al. 2013), sensory discrimination (Pinto et al. 2013; Hangya et al. 2015), associative memory (Sabec et al. 2018), and spatial (Croxson et al. 2011; Okada et al. 2015) and non-spatial working memory tasks (Furey et al. 2000; McGaughy et al. 2005; Hasselmo 2006).

To test the hypothesis, we constructed a biologically plausible model of the entorhinal-hippocampal circuit consisting of MECIII, CA1 and MEC layer V (MECV) with ACh projections from the medium septum and numerically simulated a DNMP task on a T maze. We show that the cholinergic modulation of the disinhibitory circuit in CA1 and a calcium-dependent cation

current in MEC is crucial for coordinating the encoding, maintenance and retrieval modes of the MECIII-CA1-MECV circuit. The model successfully reproduces theta phase preferences in various types of CA1 (Klausberger and Somogyi 2008) and MEC (Mizuseki et al. 2009) neurons. Further, we demonstrate whether the inactivation of MECIII-to-CA1 input may impair performance in DNMP tasks depends on the timing of inactivation, as was shown in the experiment (Yamamoto et al. 2014).

Our model also predicts that the same MECIII neurons encoding spatial information retrieve this information later, which we confirm by analyzing experimental data of single-cell and population-level activities. According to a widely accepted view, CA3-to-CA1 input is responsible for retrieving spatial memory (Middleton and McHugh 2016; Fernández-Ruiz et al. 2017). However, a few studies suggested that MECIII-to-CA1 input is engaged in the recall of spatial memory (Suh et al. 2011; Yamamoto et al. 2014), and our model supports the latter view.

Materials and Methods

Circuit structure

We built an inter-areal cortical network model with external input groups (Figure 1A). The network comprises three main areas CA1, MEC layer 3 (MECIII) and layer 5 (MECV), and includes additional areas CA3, MEC layer 2 (MECII) and the medial septum (MS) as external inputs. We built synaptic connections in our model based on anatomical observations (Witter et al. 2000; Gonzalez-Sulser et al. 2014; Unal et al. 2015). In addition, we assumed that E neurons in MECII project to PV neurons in MECIII, as previously suggested (Mizuseki et al. 2009). Connectivity across cortical areas are schematically shown in Figure 1A and detailed

parameters of the connectivity are described in “Detailed methods” in Supplemental materials.

CA1 has excitatory (E) neurons (N=480) and three interneurons: parvalbumin (PV)-positive (N=240), somatostatin (SOM)-positive oriens-lacunosum moleculare (OLM, N=240), vasoactive intestinal polypeptide (VIP, N=240) neurons. MECIII and MECV have only E and PV neurons. The numbers of E and PV neurons in ECIII are 240 and 160, respectively, while those of E and PV neurons in ECV are 400 and 120, respectively. CA3 and MECII have 480 and 120 E neurons, respectively. In MS, 360 GABAergic neurons are modeled. The GABAergic neurons in MS are divided into three groups projecting to different types of neurons in different areas, each of which has 120 neurons; groups to OLM, to PV in CA1 and to PV in MECV.

To represent the location of the model rat, we divided E neurons in CA3, CA1, MECIII and MECV into subgroups. We implemented four subgroups L, R, C and H of place cells in CA3, each of which encoded the current position of the model mouse on the left, right, center arms and at the home position, respectively (Figure 2A). Accordingly, E neurons in CA1 were also divided into four subgroups L, R, C, and H, each of which was strongly projected to by the corresponding subgroup in CA3. In contrast, MECIII and MECV had two subgroups of E neurons denoted as L and R and these subgroups were assumed to form closed loop circuits with the corresponding CA1 subgroups. Each subgroup in CA1 and MECIII had 120 neurons, while that in MECV had 200 neurons. In the present study, C and H subgroups are not necessary in MEC and we omitted these parts for the sake of simplicity. Connectivity across these subgroups is schematically shown in Figure 2A and exact parameters in the connectivity are described in

"Detailed Methods" in Supplemental materials. The other positions on the maze that are not shown in Figure 2A were not modeled in this paper.

Neuron models

Our model has two classes of neurons: i) Poisson neurons; ii) Hodgkin-Huxley type (HH) neurons.

i) Poisson neurons

There are four types of theta-oscillating neurons (excitatory neurons in CA3 and MECII, VIP neurons in CA1 and GABAergic neurons in MS) and noise neurons. Other types of neurons, that is, excitatory (E) neurons, fast spiking (PV) neurons and OLM neurons in CA1, E and PV neurons in MECIII and E and PV neurons in MECV, are modeled as HH neurons. 40 excitatory and 40 inhibitory noise neurons project to all HH neurons. Firing rates of noise neurons are different depending on the cortical areas modeled: 35 [Hz] in CA1 and MECIII and 30 [Hz] in MECV. For theta-oscillating Poisson neurons, we described the theta-oscillating (10Hz) probability of spiking per unit time $P_x(t_1 < t < t_1 + \Delta t)$ (*x*=E in CA3 and MECII, VIP in CA1, GABA in MS) as

$$P_x(t_1 < t < t_1 + \Delta t) = (\Theta(A_x\left(sin\left(2\pi\left(\frac{t}{T} - \theta_x\right)\right) + B_x\right)) + C_x)\Delta t,$$

where $\Theta(s) = s$ when *s*>0 or otherwise 0. $T = 100$ ms and $\Delta t = 0.02$ms is the step size of our numerical simulation. A_x and B_x are the amplitude and preferred phase of oscillating firing rate, respectively, and θ_x is the preferred phase of theta oscillation for the neuron type *x*, whereas C_x is the amplitude of background noise for inactive subgroups outside of their place fields. We set the preferred phases based on previous experimental studies (Borhegyi et al. 2004; Klausberger and Somogyi 2008; Mizuseki et al. 2009) as follows:

155

156 a) *x* = E in CA3

157 CA3 neurons in the model are divided into four groups according to their spatial preferences
158 (Figure 2 and Circuit structure in Materials and methods). Their firing patterns are changed
159 depending on the present location of the model rat. When the model rat is in Center ($0 < t <$
160 1000 ms, sample-C and $4500 \leq t < 7500$ ms, test-C), sample-Left ($1000 \leq t < 3000$ ms)
161 and Home ($3000 \leq t < 4500$ms) positions, Center, Left, and Home subgroups are activated,
162 respectively.

163 $A_x = 30\ [\mathrm{Hz}], B_x = 1, C_x = 0\ [\mathrm{Hz}], \theta_x = -0.2$

164 for neurons in an active subgroup, and

165 $A_x = 0\ [\mathrm{Hz}], C_x = 3\ [\mathrm{Hz}]$

166 for neurons in inactive subgroups.

167

168 b) *x* = ECII

169 During the entire trial period, we set the parameters as

170 $A_x = 5\ [\mathrm{Hz}], B_x = 0.6, C_x = 0\ [\mathrm{Hz}], \theta_x = -0.2$

171

172 c) *x* = GABAergic in MS:

173 Three groups exist in the model, those projecting to PV in CA1, to OLM in CA1 and to PV in
174 MECV. The preferred theta phase of MECV PV-projecting GABAergic neurons is the same as
175 that of CA1 OLM-projecting GABAergic neurons,

176 $A_x = 5[Hz], B_x = 2.0, C_x = 0[Hz], \theta_x = -0.5,$

177 whereas the preferred phases of CA1 PV-projecting neurons are different from the above ones
178 (Borhegyi et al. 2004) and given by

$A_x = 5[\mathrm{Hz}], B_x = 0.8, C_x = 0[Hz], \theta_x = -0.1.$

d) *x*=VIP

During the entire trial period, we set the parameters as

$A_x = 20[Hz], B_x = 0.3, C_x = 0[Hz], \theta_x = -0.4.$

e) Finally, we set a reference theta oscillation in CA1 SP as

$A_x = 1, \theta_x = 0.5, B_x = 0, C_x = 0,$

which is a virtual oscillatory component used only for determining the relative oscillation phases of other brain regions to theta oscillation in CA1 SP, but not for numerically simulating the network model. We illustrated these preference curves for all neurons in Figure 1C.

ii) HH neurons

In our model, there are seven types of neurons; E, PV and OLM in CA1, and E and PV in MECV and MECIII. all types of neurons are modeled based on previous studies as the following (See Supplemental materials for details).

We modeled excitatory neurons in CA1 based on (Wulff et al. 2009) with an afterhyperpolarization (AHP) (Middleton et al. 2008) and h (Rotstein et al. 2006) currents for generating a weak subthreshold oscillation of the membrane potentials. PV neurons in CA1, as well as those in MECIII and MECV, and OLM neurons are modeled based on (Wang and Buzsáki 1996) and (Wulff et al. 2009), respectively.

We modeled excitatory neurons in MECIII based on an excitatory neuron model of MECII (Middleton et al. 2008), with some modifications of parameter values. These neurons have an AHP current in addition to the standard sodium, potassium and leak currents. In addition, excitatory neurons in MECV are modeled based on (Egorov et al. 2002; Fransén et al. 2006) with simplification of conductance of nonspecific calcium-sensitive cationic, g_{CAN} (see Disinhibitory system in Materials and methods). Ca flux is regulated through CaL channel.

Nonlinear interaction of excitatory neurons in CA1 with input from MECIII and CA3

E neurons integrate spikes from CA3 and MECIII (Bittner et al. 2015). We introduced this effect in our model. A prolonged EPSC I_{prol} is supposed to be generated, when the following conditions are satisfied:

- An excitatory neuron in CA1 receives a burst (three spikes within 15ms) from MECIII and it does not receive any inhibitory input from OLM within 15ms at time t_1.
- This excitatory CA1 receives a burst (three spikes within 10ms) from CA3 within 20ms from t_1 (denoted t_2).
- Previous prolonged EPSC is 100ms earlier than t_2.

If these conditions are satisfied, a prolonged (100ms) EPSC is given to E neuron in CA1 according to:

$$\alpha_{prol}(t) = \begin{cases} \dfrac{t}{5} & \text{for } 0 < t < 5[ms] \\ 1 - \dfrac{t-5}{60} & \text{for } 5 < t < 35 \\ 0.5\exp\left(-\dfrac{t-35}{30}\right) & \text{for } 35 < t < 100 \\ 0 & \text{otherwise} \end{cases}$$

$$I_{prol}(t) = 0.01\alpha_{prol}(t)$$

Disinhibitory system and modulated conductance of nonspecific calcium-sensitive cationic (CAN) current through ACh.

We assume that concentration of ACh represents cognitive states and changes dependent of current locations:

$$[\mathrm{ACh}] = \begin{cases} 0.2 \text{ for } t < 1[\mathrm{s}] \text{ (a rat on sample-C)} \\ 1 - 0.8\exp\left(-\dfrac{t - T_{LS}}{200}\right) \text{ for } 1[\mathrm{s}] \le t < 3[\mathrm{s}] \text{ (a rat on sample-L)} \\ 0.8 - 0.2\exp\left(-\dfrac{t - T_{H}}{200}\right) \text{ for } 3[\mathrm{s}] \le t < 4.5[\mathrm{s}] \text{ (a rat on sample-L)} \\ 1.1 - 0.3\exp\left(-\dfrac{t - T_{CT}}{200}\right) \text{ for } 4.5[\mathrm{s}] \le t \text{ (a rat on test-C)} \end{cases}$$

[ACh] modifies neural behavior in a circuit in two pathways. Efficacy of connections from VIP is modified with [ACh] (Circuit structure in Materials and methods) as well as conductance of I_{CAN}. A channel of I_{CAN} takes high and low conductance states alternatively. Maximum conductance g_{CAN} is determined by [ACh] and ratio of high conductance state r_{h}. r_{h} is dependent on history of [Ca2+] and [ACh] (Fransén et al. 2006) as follows:

$$g_{CAN}(t) = 0.5[Ach] r_{\mathrm{h}}(t)$$

$$r_{\mathrm{h}}(t + \Delta t) = \begin{cases} r_{\mathrm{h}}(t) + 0.6\Delta t \text{ for } [Ca^{2+}] > 0.004 \\ r_{\mathrm{h}}(t) - 0.08\Delta t \text{ for } [Ca^{2+}] < 0.0003 \\ r_{\mathrm{h}}(t) \quad \text{otherwise} \end{cases}$$

We also set upper and lower bounds for r_{h} at 1 and 0.12, respectively.

An additional decoder which is a downstream of MEC-CA1 circuit

To examine how high gamma coherence between MECIII and CA1 observed in (Yamamoto et al. 2014) is utilized for detection of previous memories, we applied stimuli with high gamma oscillation to these areas and implemented an additional circuit as a decoder. The decoder circuit composes 100 excitatory (exc) and 100 inhibitory (inh) neurons (Figure 9A) which

receive synaptic inputs from excitatory neurons in MECIII and CA1. See Neuron model and circuit structure in the additional decoder in Supplemental materials for details. For the high gamma stimuli, we applied coherent current input $I_{\text{high }\gamma}$ to excitatory neurons in CA1 and ECIII with f=80 Hz as follows:

$r_t = \sin(2\pi f t/1000)$, here *t*=*t*[ms],

$$I_{\text{high }\gamma} = \begin{cases} 0.02 m r_t \text{ for } m r_t > 0 \\ I_0 r_t \text{ for } r_t \leq 0 \end{cases},$$

$I_0 = 0.18$ for CA1 neurons, 0.216 for ECIII neurons.

Periodicity analysis

Neural activity in the model oscillates driven by external theta rhythm (10Hz). We evaluated how strongly neurons oscillate in the theta rhythm by calculating an autocorrelation function R(t) (Yamamoto et al. 2014). Periodicity index is defined as $\max_{50\text{ms}<t<200\text{ms}} R(t)$.

Experimental data in rodents

Spiking activities and LFP data in CA1 are obtained from previously published data in (Yamamoto et al. 2014) for Figures 6B and 7C and that in (Mizuseki et al. 2013) for Figures 6D and 6E. Experiments were approved by the Institutional Animal Care and Use Committee of Rutgers University. All procedures for animal care and use were performed in accordance with the National Institutes of Health Guide for the Care and Use of Laboratory Animals. Detailed conditions on data recording are described in these papers.

LFP activities were band-pass filtered (6-12Hz) as theta wave and instantaneous phase of the filtered theta wave were derived from Hilbert transform. For spiking activities, we dropped a part of spikes to analyzed as follows:

Spiking activities in (Yamamoto et al. 2014) were recorded with the silicon linear probes and were analyzed as multi-unit activities. In this paper, however, we roughly distinguish putative excitatory neurons from inhibitory ones in order to show clear theta preference. According to (Mizuseki et al. 2009), we sorted spikes by trough to peak latency. Due to short length of single spike profile in the data, we cannot identify baseline before spike and consequently cannot compute peak amplitude asymmetry. We assigned spikes with the latency larger than 0.5ms to putative excitatory neurons. For Figure 7B, we have the sorted spikes in three out of five rats because spikes of the rest two rats do not show clear theta preference due to small number of spikes.

For spiking activities in (Mizuseki et al. 2013), we used sessions "ec014.12","ec014.16","ec014.17","ec014.27","ec014.28","ec013.44","ec013.46","ec016.30". Because phase shift in the side arm was observed only in deeper neurons in (Fernández-Ruiz et al. 2017), we only used spikes of deeper neurons according to (Mizuseki et al. 2011).

Calculations of the ratio of spikes at the peaks in theta and the side-to-center ratio

In Figure 7F, we used the same neurons in Figure 7E (see Experimental data in rodents). Further, we filtered these neurons by two criteria: i) number of spikes in the later center arm are larger than 50; ii) the ratio of spikes in the later center arm to total spikes is larger than 5%. To exclude place cells representing the earlier center arm and junction of T-maze (since these cells are likely to spike at the peaks in theta oscillation in the later center arm), we further excluded the cells that spike in the later center arm less frequently than at the earlier

center arm or the junction. Eleven neurons remained. For these neurons, we calculated the ratio in number of spikes around the peaks (90-270 degree) to all spikes in the later center arm. We call this quantity the ratio of spikes at the peaks. We also calculated the ratio of average number of spikes emitted in the later center arm to that of average number of spikes emitted in the side arms. We call this quantity the side-to-center ratio.

Results

Hippocampus-entorhinal cortex circuit model

To clarify the circuit mechanisms to control flexibly spatial information in the hippocampus and MEC, we built an inter-areal cortical network model (Figure 1A, see "Circuit structure" in Materials and Methods). The network comprises three main areas CA1, MECIII and MECV, and includes additional areas CA3, MECII and MS as external inputs. These external inputs oscillate at theta frequency (10Hz) and entrain the main circuit to theta-frequency oscillation. CA3 neurons encode the current location of model rat and transfer the location information to CA1. All main areas have excitatory (E) and inhibitory PV neurons. In addition to these neurons, the model CA1 has OLM and VIP neurons.

Acetylcholine (ACh) is known to modulate activity of VIP neurons (Albuquerque et al. 2009) and the conductance of calcium-sensitive non-specific cation current (CAN) in MECV excitatory cells (Fransen et al. 2002; Fransén et al. 2006). The concentration of ACh ([ACh]) is generally thought to change in a diffusive and tonic manner on slow timescales of minutes or hours. However, recent studies have revealed that [ACh] undergoes rapid phasic changes on sub-second and second timescales (Parikh et al. 2007; Zhang et al. 2010; Teles-Grilo Ruivo et

al. 2017). In this study, we assumed that [ACh] varies in correlation with cognitive demands, i.e., [ACh] is high, slightly lowered and again high during encoding, maintenance and recalling of working memory, respectively. In contrast, the default concentration of ACh is low (Figure 1B). In reality, these cholinergic modulations may be induced by MS (Zhang et al. 2010; Newman et al. 2012; Okada et al. 2015), but cholinergic neurons in MS were not explicitly modeled in the present study. Under this model setting, we tested the hypothesis that ACh controls information flow across the entorhinal-hippocampal loop circuit in the different cognitive epochs of a DNMP task. In particular, we proposed and explored the possibility that [ACh] regulates the disinhibition of CA1 E neurons and the calcium dynamics in MECV E neurons to enable the flexible processing of spatial working memory.

Before showing the details of our network model, we schematically explain the mechanisms of spatial working memory which we intend to propose in this study (Figure 1B). In the default epoch (before encoding), [ACh] is low and activity of PV is high enough to inhibit activity of CA1 E neurons and the flow of information on the current location from CA3 to CA1 (shaded arrow in the panel of default epoch). In the encoding epoch, [ACh] is set higher and consequently VIP neurons are activated, which in turn inhibits CA1 PV neurons to enable the transfer of location information into CA1. Thus, the location information is stored in the CA1-MECV-MECIII loop circuit (magenta arrows in the panel of encode epoch). Next, in the maintenance epoch, [ACh] is at a middle level and PV neuron activity is again high, blocking the re-entry of location information into CA1. Despite this blockade, however, the spatial information is maintained by the activation of calcium-dependent cation current in MECV E neurons without spike generation. We assume that the current remains activated at the modest level of [ACh]. Finally, in the decoding epoch, [ACh] is high again and information on

Figure 1

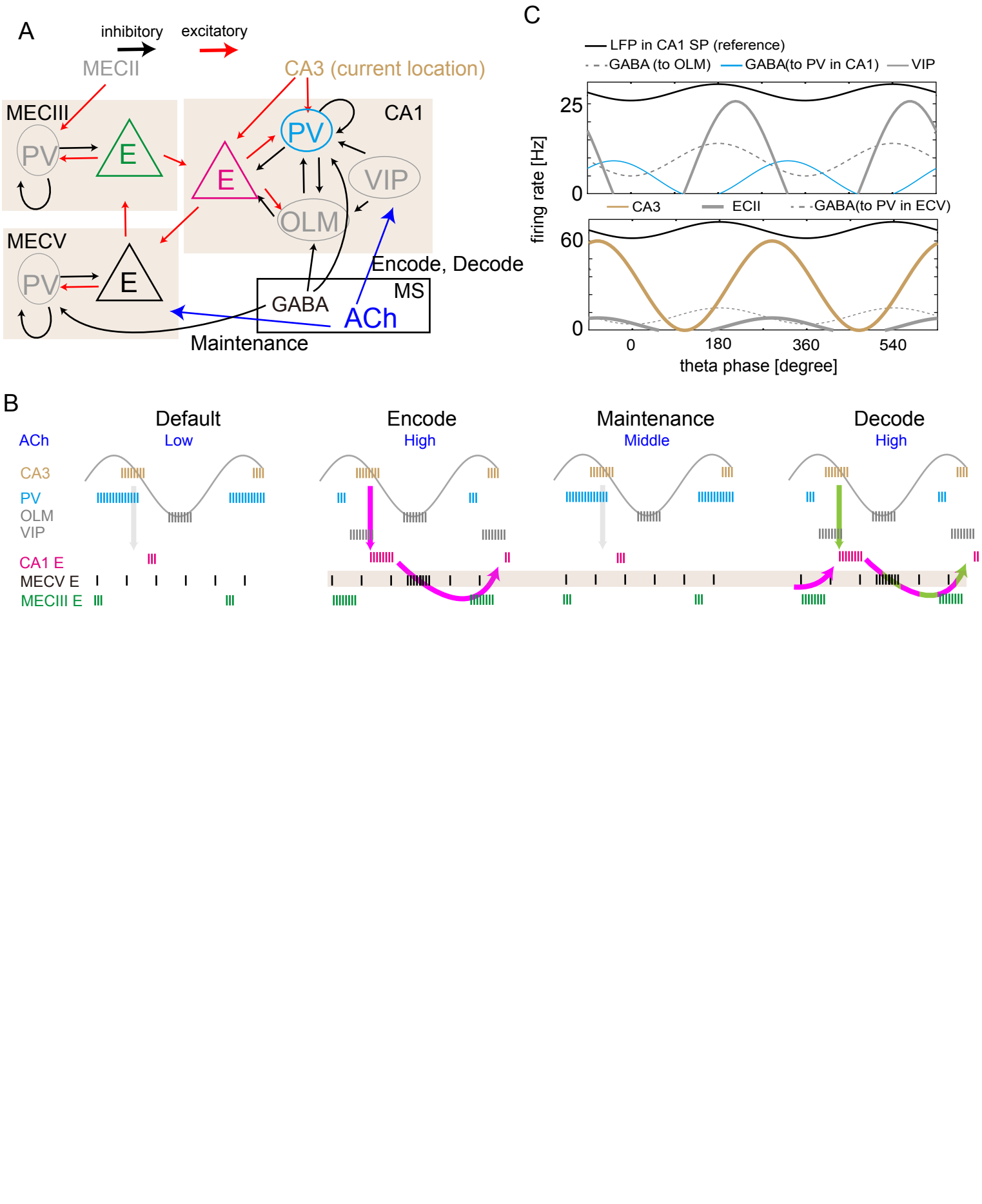
A
inhibitory
excitatory
MECII
CA3 (current location)
MECIII
CA1
PV
E
VIP
OLM
MECV
Encode, Decode
MS
GABA
ACh
Maintenance
C
LFP in CA1 SP (reference)
GABA (to OLM)
GABA(to PV in CA1)
VIP
CA3
ECII
GABA(to PV in ECV)
firing rate [Hz]
theta phase [degree]
B
Default
Encode
Maintenance
Decode
ACh
Low
High
Middle
High
CA3
PV
OLM
VIP
CA1 E
MECV E
MECIII E

Figure 1. Entorhinal-hippocampal network model (A) Connectivity of the network model is shown. E: excitatory neurons, PV: parvalbumin (PV)-positive neurons, OLM: somatostatin (SOM)-positive oriens-lacunosum moleculare neurons, VIP: vasoactive intestinal polypeptide neurons, ACh: acetylcholine neurons. ACh regulates VIP to control CA1 E during encoding and decoding epochs and modulate sensitivity in MECV E during encoding, maintenance and decoding epochs. (B) Schematic image of the proposed mechanisms of spatial working memory. Vertical lines represent spikes of each neuron. Sinusoidal curve indicates theta oscillation in the CA1 stratum pyramidale (SP) layer. As described in C, this theta oscillation was used for a reference frame to measure the preferred phases of neuronal firing in our model. See the main text for details. (C) Theta-modulated firing probability densities of input neurons are schematically shown during the sample-center run. The preferred firing phases were determined with respect to a reference theta oscillation (black) reported in the CA1 SP. These given preferred phases in input result in preferred phases in neurons within the circuit consistent with the empirical observations (See Figure S1).

the current location is loaded from CA3 to CA1 (green arrow). It is noted that information on the previous location maintained in MECV is also re-loaded from MECIII to CA1. Therefore, CA1 exhibits both current and previous position-encoding activities in the decoding epoch.

The core circuits of the present network model consist of E, PV and OLM neurons, which were modeled as Hodgkin-Huxley-type conductance-based neurons (See “Neuron models” in Materials and Methods). VIP neurons were modeled as Poisson firing neurons with a probability density of spikes and their outputs reflect the modulatory effect of ACh. We described CA3 E neurons projecting to CA1, MECII E neurons projecting to MECIII, and GABAergic neurons in MS projecting to CA1 and MECV as external Poisson spike trains. As shown in Figure 1C, the firing probabilities of these neurons were modulated at the theta-band frequency (10 Hz) to induce theta rhythmic activities in the core circuits. The relative preferred theta phases of the external inputs were chosen such that the preferred phases of various model neurons are consistent with experimental observations (Klausberger and Somogyi 2008; Mizuseki et al. 2009). Furthermore, the relative phases between these inputs and theta oscillation in CA1 are experimentally known, from which we can define the theta phase of the local field potential (LFP) to be observed in the stratum pyramidale (SP) of CA1. This LFP oscillation was used as a reference to measure the degree of agreement between the preferred phases of model neurons and experimental observations. The preferred phases of GABAergic neurons in MS were dependent on their target neuron types (ECV PV, CA1 PV and CA1 OLM). In experiment, GABAergic neurons projecting to OLM and those projecting to PV in CA1 have different preferred phases (Borhegyi et al. 2004).

359 Given these settings of external theta-rhythmic sources, in a default epoch the resultant firing
360 of all neurons in CA1, MECIII and MECV showed theta-rhythmic patterns and their preferred
361 phases are consistent with experimental observations (Figure S1): E and OLM neurons in CA1
362 showed preferred phases around the troughs of theta oscillation, whereas PV neurons around
363 the peaks (Klausberger and Somogyi 2008). In MECIII, E and PV neurons fired preferentially
364 around the peaks and troughs of theta oscillation, respectively (Mizuseki et al. 2009). In MECV,
365 PV neurons preferred the troughs, but E neurons did not show strong phase preferences
366 (Mizuseki et al. 2009). Thus, the model neurons show biologically plausible theta-phase
367 locking activity.
368
369 **Encoding and recalling of spatial information in the circuit model**
370 The central question of this study is to clarify how spatial information is encoded, maintained
371 and recalled in the entorhinal-hippocampal circuits. Before studying this problem, we, first,
372 asked whether our model can replicate the task-related activities reported in previous
373 experiments. In particular, we considered a DNMP task on a T-maze (Yamamoto et al. 2014).
374 In this experiment, one arm of the T-maze was closed during a sample run and the mouse was
375 forced to choose another arm. After a delay period, the mouse was set to a test run in which
376 both arms were open and the mouse had to choose the arm opposite to the one chosen in
377 the preceding sample run (that is, if the mouse chose the right arm in the sample run, it had
378 to choose the left arm in the test run). For a successful test run, the mouse had to remember
379 the previously chosen arm. This task requires at least two types of memory, namely, rule-
380 based memory and spatial working memory. The former memory is thought to be encoded in
381 the prefrontal cortex (Durstewitz et al. 2010; Preston and Eichenbaum 2013; Guise and

382 Shapiro 2017). However, in this study we did not model the prefrontal circuits and focused on
383 the processing of spatial working memory in the entorhinal-hippocampal circuits.
384
385 Figure 2A shows the organization of sample and test runs in our model together with the
386 connectivity patterns between the neural ensembles encoding different locations on the maze.
387 We monitored the activity of sample runs along the center arm (sample-C) and left arm
388 (sample-L), and that of test runs at the home position (delay) and center arm (test-C) up to
389 the junction (decision point) of the T-maze. For the sake of simplicity, we implemented four
390 subgroups L, R, C and H of place cells in CA3, each of which encoded the current position of
391 the model mouse on the left, right, center arms and at the home position, respectively. For
392 instance, neurons belonging to the subgroup L were given a higher firing probability when the
393 model mouse traveled across the left arm (Figure 2B; also see "Neuron models" in Materials
394 and methods). Accordingly, E neurons in CA1 were also divided into four subgroups L, R, C,
395 and H, each of which was strongly projected to by the corresponding subgroup in CA3. In
396 contrast, MECIII and MECV had two subgroups denoted as L and R and these subgroups were
397 assumed to form closed loop circuits with the corresponding CA1 subgroups. Detailed
398 connectivity in these groups is described in “Network structure” in Materials and Methods.
399
400 Below, without loss of generality, we consider the case that the mouse chooses the left arm
401 in every sample trial. Accordingly, we define decoding ability as the probability of Left choice,
402 P_L, which is estimated as $P_L = e^{-r_L}/(e^{-r_L} + e^{-r_R})$, where r_L and r_R are the spike rates of the
403 L and R subgroups, respectively, during the test-C period. Note that P_L can be written as a
404 function of $r_L - r_R$. The larger the difference in the spike rates, the more robust the memory
405 encoding.

Figure 2

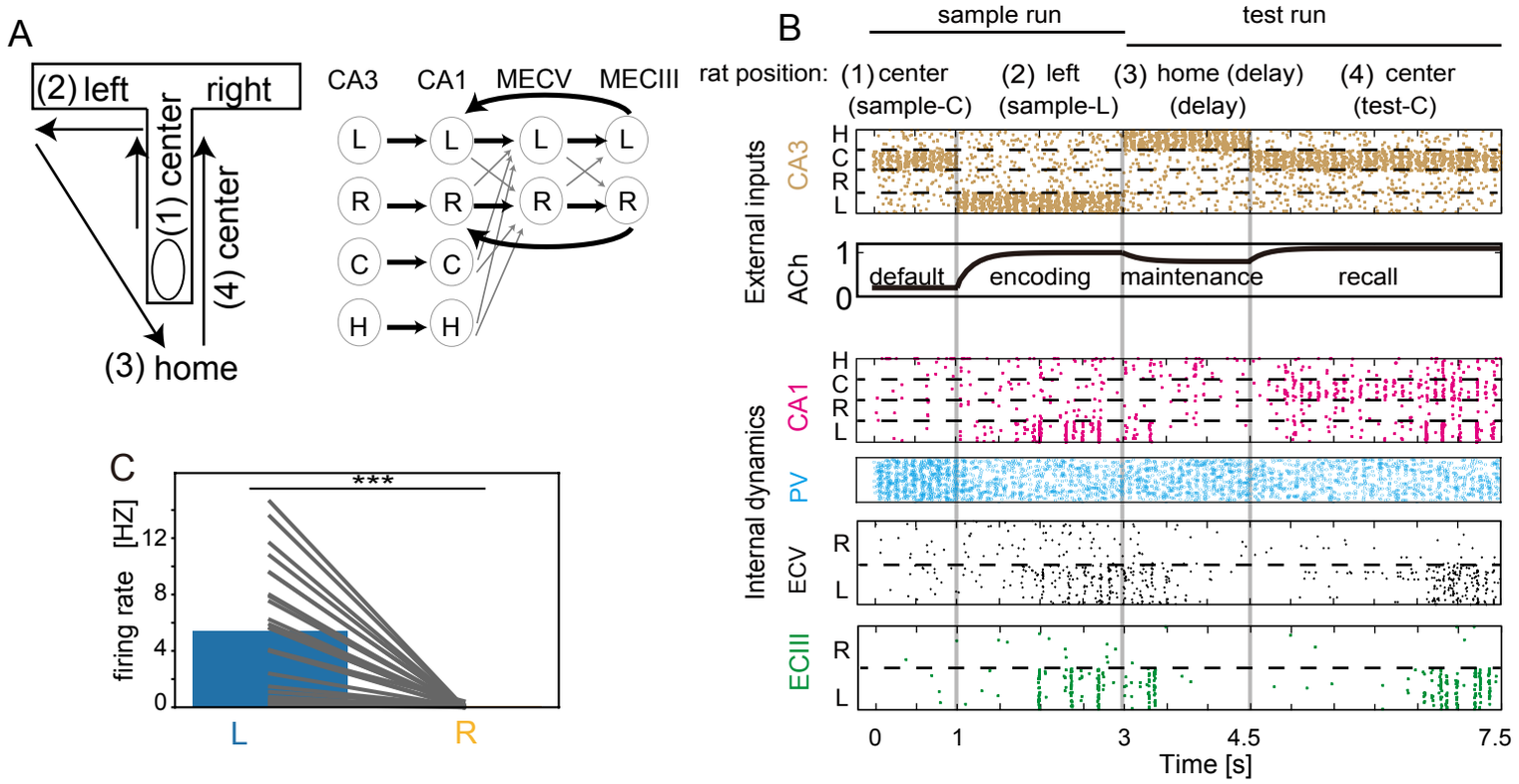
A
(2) left
right
(1) center
(4) center
(3) home
CA3
CA1
MECV
MECIII
L
R
C
H
B
sample run
test run
rat position: (1) center (sample-C)
(2) left (sample-L)
(3) home (delay) (delay)
(4) center (test-C)
External inputs
CA3
ACh
default
encoding
maintenance
recall
Internal dynamics
CA1
PV
ECV
ECIII
Time [s]
C
firing rate [HZ]
***

Figure 2. Performance of the model for a DNMP task (A) Left; Schematic illustrations of task periods during the sample and test trials of the DNMP T-maze task: (1) center in the sample trials (sample-C), (2) left in the sample trials (sample-L), (3) home (delay), (4) center in the test trials (test-C) periods. Right; Synaptic connectivity is shown between the neuron subgroups encoding the specific locations of the maze (left, right, center arms and home position). Connections (bold) are stronger within the loop circuit of MECV, MECIII and CA1 than other modest connections (solid). (B) Raster plots of E neurons in different cortical areas are shown together with the time evolution of ACh concentration. (C) The average firing rates of MECIII L and R subgroups were calculated for the test-C period in 25 runs of simulations (black lines, five different networks with five different initial conditions). Unless otherwise stated, average firing rates were evaluated in a similar fashion throughout this study.

In experiment, coherence between MECIII and CA1 increased in the high-gamma band (60-120Hz) as the animal approached the junction point on the T-maze (Yamamoto et al. 2014). The result indicates that high-gamma oscillation plays an active role in the decision making, presumably in reading out stored locations from working memory. However, the task performance of the animal was also highly correlated with theta-phase-locked firing in MECIII. In addition, as shown later, our model successfully performs working memory tasks without gamma oscillation. We speculate that high-gamma oscillation nested in theta oscillation may either help the downstream areas (responsible for the generation of behavioral outputs) to correctly read out the stored locations from the entorhinal-hippocampal circuit or mediate top-down signals to shift the status of the entorhinal-hippocampal circuit from the maintenance mode to the readout mode. Because, in this study, we focus on spatial information processing within CA1 and MEC, we will minimally model a downstream area of the entorhinal-hippocampal circuit to analyze the effect of the high-gamma coherence on working memory performance.

Implications of preferred theta phases in coordinating activities in the CA1-MECV-MECIII loop circuit

In Figure 2B, we show activities of E neurons in CA3, CA1, MECV and MECIII together with [ACh] during (1) sample-C, (2) sample-L, (3) home (delay) and (4) test-C runs. Depending on the mouse's position, the corresponding subgroup was activated in CA3 according to the given firing probability. During the sample-L run, [ACh] was set to increase, which disinhibited CA1 PV neurons and accordingly strongly activated the CA1-MECV-MECIII loop circuit of the L subgroups to encode a choice memory in MECIII. Then, in the delay period, [ACh] was set to

decrease slightly, which strongly suppressed neural activities in all L subgroups including the CA1 subgroup L. We note that a similar suppression arose in experiment as if spatial memory had not been maintained during delay periods (Yamamoto et al. 2014). During the test-C run, the CA1 subgroup C was activated driven by the CA3 subgroup C. Importantly, as the model mouse approached to the decision point, the subgroups L were gradually reactivated in the loop circuit to retrieve the memory of the previous choice. This activation-suppression-reactivation pattern is clearly seen in the firing rate of MECIII neurons. Average firing rates during the test-C period were significantly different ($p=3.071 \times 10^{-6}$, *t* test on two related samples) between the subgroups L and R in MECIII (Figure 2C), implying that the network model successfully recalled the stored spatial memory.

The successful encoding of memory required theta-phase-locking of neural firing along the CA1-MECV-MECIII loop circuit. As mentioned previously, the theta phases of external sources (i.e., CA3, MECII and MS) entrain neurons in these areas in theta-phase-locked firing with the preferred phases that are consistent with experimental observations. In the normal situation, MECIII PV neurons are activated by input from MECII at the troughs of theta oscillation and consequently MECIII E neurons tend to fire at the peaks. Then, CA1 E neurons are strongly activated in a nonlinear manner(Takahashi and Magee 2009; Bittner et al. 2015) by near-coincident inputs from MECIII and CA3: spikes from CA3 arriving at CA1 just after spikes from MECIII activate CA1 E neurons much stronger than those from CA3 arriving at otherwise timing (see Materials and methods).

All model neurons oscillate at theta frequency due to theta-rhythmic external inputs. Is theta modulation necessary for successful working memory function in our model? To answer this,

we changed the strength of theta modulation in all the external inputs and examined how network behavior is affected by these changes (Figure 3A). Figure 3B shows the normalized difference between the firing rates in L and R subgroups in CA1 during the encoding epoch. Reduced amplitudes of theta modulation led to smaller differences between the firing rates, degrading the decoding ability as indicated by smaller P_L values in Figures 3C and 3F. These results demonstrate the importance of theta modulation in working memory function.

We then explored whether decoding ability also depends on the coordination of relative theta phases of external inputs. The theta phases of inputs from the different sources were tuned in the model such that they are consistent with experimental observations (Figure 1C). To examine the functional implications of this temporal coordination, we shifted the preferred phases of MECII neurons by 180 degrees from the troughs to the peaks of the reference theta oscillation of CA1 LFP (Figure 3D). Figure 3E shows the phase preferences of CA3, CA1 E, CA1 PV, and MECIII E neurons after this change. MECIII PV neurons dramatically reduced spikes at the descending phases of theta oscillation, which shifted the firing of MECIII E neurons to the troughs of theta oscillation. Consequently, the peak activities of MECIII and CA3 were separated by about one half of theta cycle and did not coincidently innervate CA1. The timing deviation impaired the encoding of spatial information into the loop circuit, as indicated by reduced rate differences between L and R subgroups, resulting in a degraded decoding ability (Figure 3F, $p= 2.334 \times 10^{-8}$, *t* test on two related samples). Thus, the specific coordination of the preferred theta phases of MECIII and CA3 neurons is crucial for the working memory operation of the entorhinal-hippocampal circuit.

The role of disinhibition in regulating the activity of the CA1-MECV-MECIII loop circuit

Figure 3

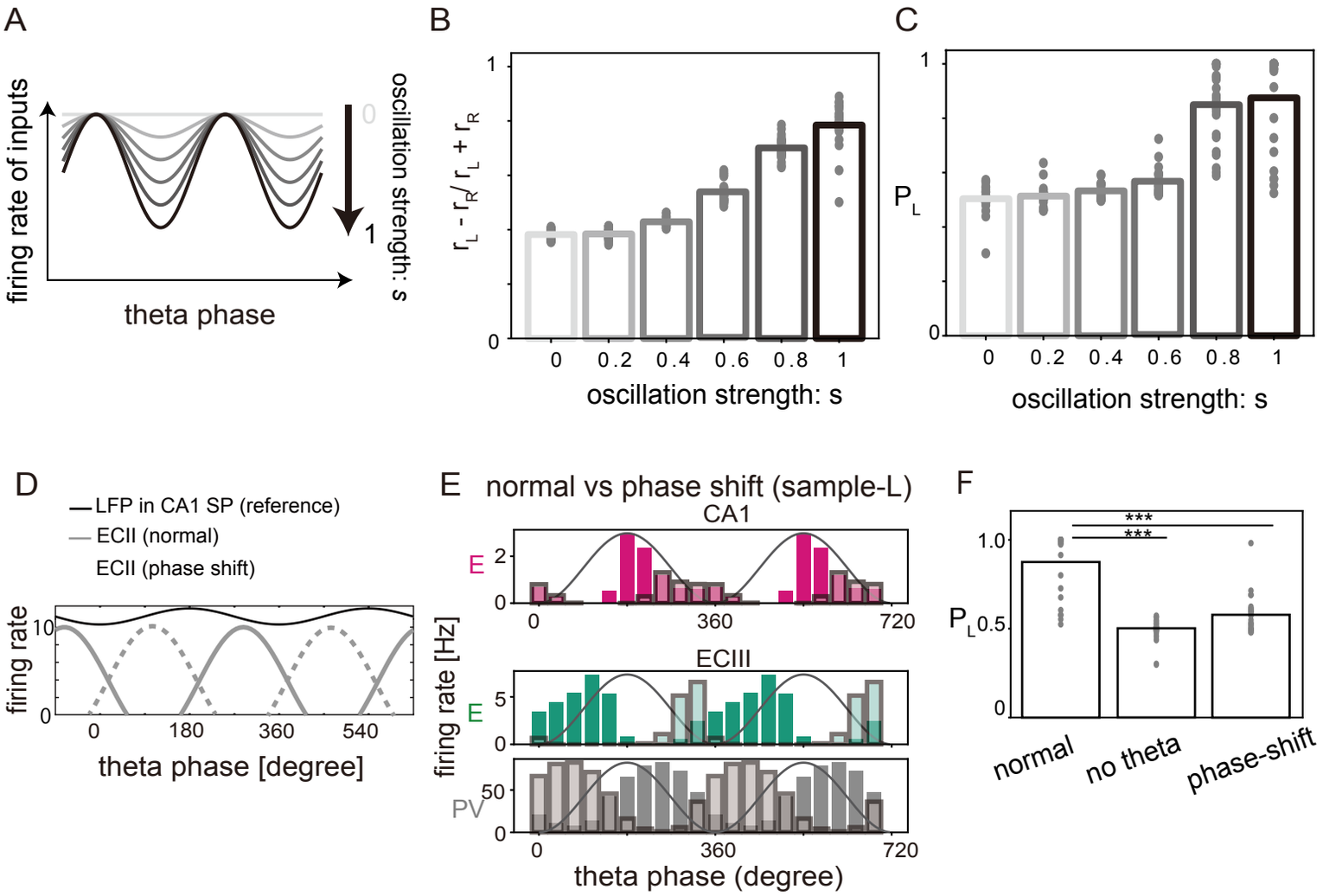
A
firing rate of inputs
theta phase
oscillation strength: s
0
1
B
$r_L - r_R / r_L + r_R$
oscillation strength: s
C
P_L
oscillation strength: s
D
LFP in CA1 SP (reference)
ECII (normal)
ECII (phase shift)
firing rate
theta phase [degree]
E
normal vs phase shift (sample-L)
CA1
ECIII
PV
firing rate [Hz]
theta phase (degree)
F
***
***
P_L
normal
no theta
phase-shift

Figure 3. Theta oscillation plays a critical role on the performance. (A) Schematic image of change in oscillation strength *s* in theta rhythmic inputs. *s*=1 corresponds to the normal case, while *s*=0 does to no theta rhythm case. (B) Normalized differences in the firing rates between the L and R subgroups of CA1 E neurons were calculated during the sample-L period for different *s*. The difference for all of the weaker rhythmic input cases are significantly reduced compared to that for the normal case ($p=4.00\times10^{-18}$, 3.49×10^{-18}, 3.52×10^{-17}, 1.59×10^{-12}, 0.00051 for *s*=0, 0.2, 0.4, 0.6, and 0.8, respectively, *t* test on two related samples). (C) Probability of left choice (P_L) and average of P_L were calculated during the test-C2 for different *s*. P_L is also reduced significantly for *s*=0, 0.2, 0.4, and 0.6 ($p=8.00\times10^{-10}$, 3.66×10^{-10}, 1.30×10^{-9}, 4.44×10^{-9}, respectively, *t* test on two related samples) from the normal case, but not reduced for *s*=0.8 (p=0.553, *t* test on two related samples). Gray dots show values of different networks for different initial conditions and bars are mean values. Chance level is 0.5. Unless otherwise stated, P_L was evaluated in a similar fashion throughout this study. (D) Theta-modulated firing probabilities of ECII neurons for the normal and preferred phase shift conditions are shown. (E) Modulations of spike counts by theta oscillation are shown for CA1 E, MECIII E and MECIII PV neurons during the sample-L period. Neuronal activities in the normal and preferred phase shift conditions of theta oscillation are shown with dark and light colors, respectively. (F) P_L was calculated in the normal, no theta modulation and phase-shift conditions.

We show that the ACh-mediated disinhibitory mechanisms regulate cross-area communications within the entorhinal-hippocampal circuit during different task periods. We first analyzed how activity of CA1 E neurons is regulated by [ACh]. We consider the default epoch (i.e., 0 to 1 sec in Figure 2B) in which [ACh] is low (Figure 4A). In this epoch, output from VIP neurons is weakened and, consequently, PV and OLM neurons are strongly activated around the peaks and the troughs of theta oscillation, respectively (Figure 4B). Accordingly, CA1 E neurons rarely fire around the peaks and troughs (but they can generate a small number of spikes driven by external noise after the troughs of theta oscillation at which inputs from both PV and OLM are weakened: see Figure S1). In contrast, during the epochs of high [ACh] (Figure 4D, the sample-L period: the test-C period also corresponds to the high [ACh] epoch, but will be discussed later), CA1 E neurons show strong activation immediately after the peaks of theta oscillation because PV neurons are suppressed around the peak (Figure 4E). OLM neurons are also suppressed, but their inhibitory effect on E-neuron firing around the peak is relatively weak (the effects of PV and OLM are analyzed below). Thus, [ACh] regulates the activity of CA1 E neurons. Also, the cholinergic modulation advances the preferred phase of CA1 E neurons from the troughs to the peaks of theta oscillation. Later, we will examine the model's prediction in experimental data.

Next, we asked if information on the current position of the mouse can be selectively transferred from CA3 to CA1 by [ACh]. Although, throughout the task, CA1 E neurons constantly receive position information from CA3, a certain mechanism is required to transfer CA3 position information to CA1 neurons selectively during encoding epoch (in the sample-L period, see the CA1 L subgroups in Figure 2B). We found that ACh-induced disinhibition provides this mechanism: at the sample-C period [ACh] is low and the sensitivity of CA1 E

Figure 4

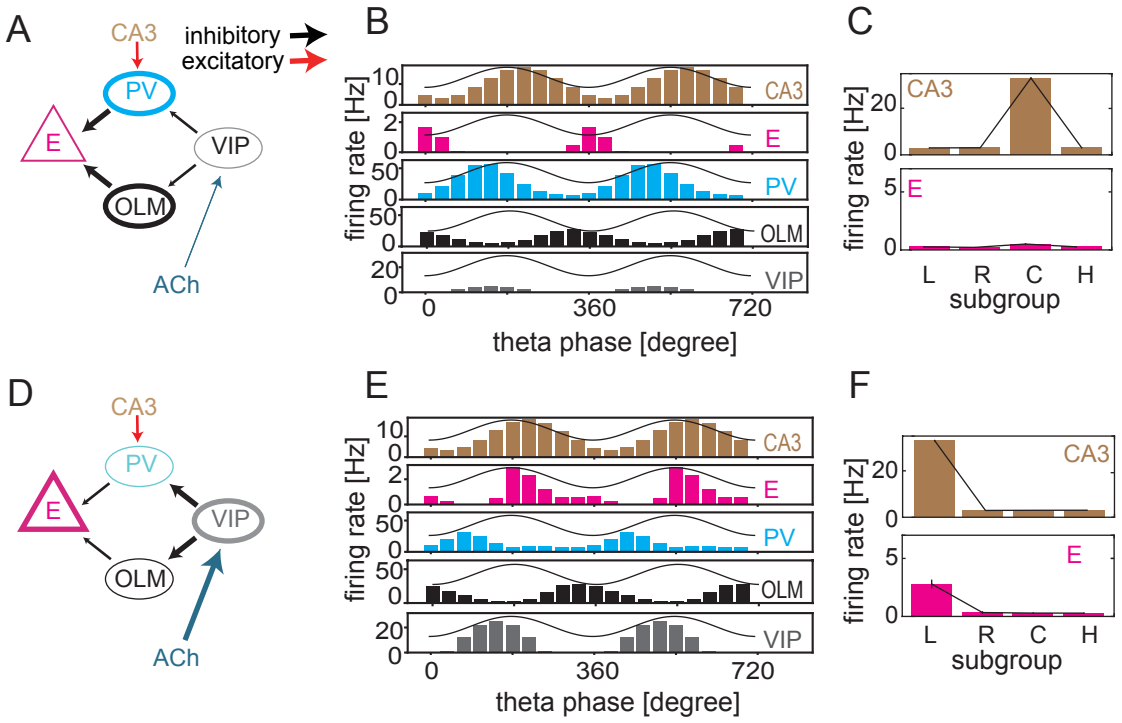
A
CA3
inhibitory
excitatory
PV
E
VIP
OLM
ACh
B
firing rate [Hz]
CA3
E
PV
OLM
VIP
0
360
720
theta phase [degree]
C
CA3
E
firing rate [Hz]
L
R
C
H
subgroup
D
CA3
PV
E
VIP
OLM
ACh
E
firing rate [Hz]
CA3
E
PV
OLM
VIP
0
360
720
theta phase [degree]
F
CA3
E
firing rate [Hz]
L
R
C
H
subgroup

Figure 4. Gating of CA3-to-CA1 signaling by disinhibition mechanism. (A) The operation mode of disinhibitory circuit is schematically illustrated in low [ACh] states. (B) Theta phase preferences of spikes during the sample-C period are shown for CA1 neurons including all subgroups. Only for VIP neurons, the firing rate normalized by [ACh], which corresponds to output from VIP neurons to other inhibitory neurons (see the Materials and methods), is plotted. Solid curves show the reference theta oscillation. (C) Average firing rates of the L, R, C and H subgroups in CA3 and CA1 are shown during the sample-C period. Error bars indicate s.d. (D) The operation mode of disinhibitory circuit in high [ACh] states. (E, F) Similar to (B) and (C) during the sample-L period.

neurons to CA3 input remains low, consequently the position information is not transferred to CA1 (Figure 4C); at the sample-L period [ACh] is increased and accordingly the sensitivity is also enhanced, resulting in an information transfer (Figure 4F).

The disinhibition mechanism further explains why the blockade of MECIII-to-CA1 connections impaired task performance in the experiment (Yamamoto et al. 2014). When the model mouse is sampling left or right arm, the disinhibition mechanism enables the activation of the corresponding subgroups in the CA1-ECV-ECIII loop: highly activated CA1 neurons activate MECV E neurons, which in turn activate MECIII E neurons. MECIII-to-CA1 projections further activate CA1 E neurons, thus completing a positive feedback loop within the activated subgroups. However, the blockade of MECIII-to-CA1 connections reduces neural activity in CA1 and hence in MECIII, disabling the storage of the current position.

To confirm the crucial roles of disinhibition (i.e., VIP-PV-E and VIP-OLM-E connections) in the working memory task, we studied three cases. In the first case, PV neurons were inactivated in CA1 during the entire trial period without changing the other conditions (Figure S2A). Due to the lack of inhibition from PV neurons, CA1 E neurons were strongly activated at any ACh concentration. In the encoding epoch, E neurons exhibited higher activity in the L subgroup than in the R subgroup in both CA1 (Figure S2B) and ECIII (Figure S2C, 1 to 3 sec). However, after this epoch E neurons immediately lost selectivity to spatial information because they were too strongly activated in both subgroups. During some intervals firing rate was higher in the L subgroup than in the R subgroup, but it was opposite during other intervals (Figure S2C, after 3 sec). Thus, the spatial information recalled randomly varied from trial to trial, and working memory performance was unreliable (Figure S2H).

In the second case, the cholinergic modulation of PV neurons (but not that of OLM neurons) was terminated during the entire trial period. In this case, PV neurons were not inactivated even at high [ACh] (Figure S2D) and the encoding of spatial information into CA1 was largely impaired (Figure S2E). Consequently, spatial information could not be stably maintained in MECIII (Figure S2F) and probability of left choice, P_L, was significantly decreased (Figure S2H, $p=1.542\times10^{-9}$, *t* test on two related samples). Thus, in both cases, spatial information in CA3 was not successfully transferred into the CA1-MECV-MECIII loop circuit.

In the third case, OLM neurons were inactivated during the entire trial period. OLM neurons innervate both E and PV neurons in CA1. Consequently, OLM neurons exert both excitatory and inhibitory effects on CA1 E neurons during one cycle of theta oscillation. We found that the inactivation of OLM neurons reduces the difference in firing rate between L and R subgroups in CA1 (Figure S2G) and impairs working memory performance (Figure S2H). We, however, note that this impairment is less serious than that caused by the inactivation of PV neurons. This was because the preferred phase of OLM neurons is the trough of theta oscillation (i.e., fewer spikes around the peak in Figure 4E than in Figure 4B) at which excitatory neurons rarely fire in the intact network model.

Covert activation by calcium dynamics

An unexpected experimental finding was that neural activities in MECIII were strongly suppressed during delay periods (Yamamoto et al. 2014). This observation challenges our hypothesis that either MECV or MECIII, or both, serve for working memory in the spatial decision making task, raising the question about how the entorhinal-hippocampal circuit

recalls the encoded spatial information after the delay periods. To explore the underlying circuit mechanisms of memory recall, we implemented calcium-sensitive non-specific cation current (CAN current in Materials and methods) in our cortical neuron models.

The CAN current was originally proposed to explain persistent activity of single cortical neurons in MECV (Fransen et al. 2002; Fransén et al. 2006), and a similar persistent activity was later shown in the layer V of various cortical areas (Rahman and Berger 2011). The CAN current is activated in the presence of ACh with the intensity depending on the activation rate of high conductance channels, r_H. The conductance r_H increases in time when the calcium concentration $[Ca^{2+}]$ is beyond a critical value d_P and decreases when $[Ca^{2+}]$ is below another critical value d_D. Because $d_D < d_P$, a hysteresis effect or bistability appears for $d_D < [Ca^{2+}] < d_P$. Thus, once $[Ca^{2+}]$ exceeds d_P, the value of r_H remains high until $[Ca^{2+}]$ again decreases below d_D (Figure 5A). Neurons with high r_H respond to input more sensitively than those with low r_H and, thus, memory of previous high activity is stored in r_H through calcium dynamics.

In the sample-L period, an increased activity of the CA1 subgroup L enhanced spike firing of MECV E neurons in the subgroup L (Figure 5B). During the enhanced firing, $[Ca^{2+}]$ was elevated in these neurons by calcium influx through the voltage-dependent calcium channel. This increase of $[Ca^{2+}]$ occurred only in the MECV subgroup L but not in the MECV subgroup R (Figure 5C). After the sample-L period, [ACh] was decreased and, consequently, the CAN current was also decreased. Because lowering [ACh] decreased the output of VIP neurons, that of PV neurons was increased and consequently that of CA1 E neurons was suppressed. Thus, the changes in neural activity resulted in a decreased firing rate of MECV E neurons.

Figure 5

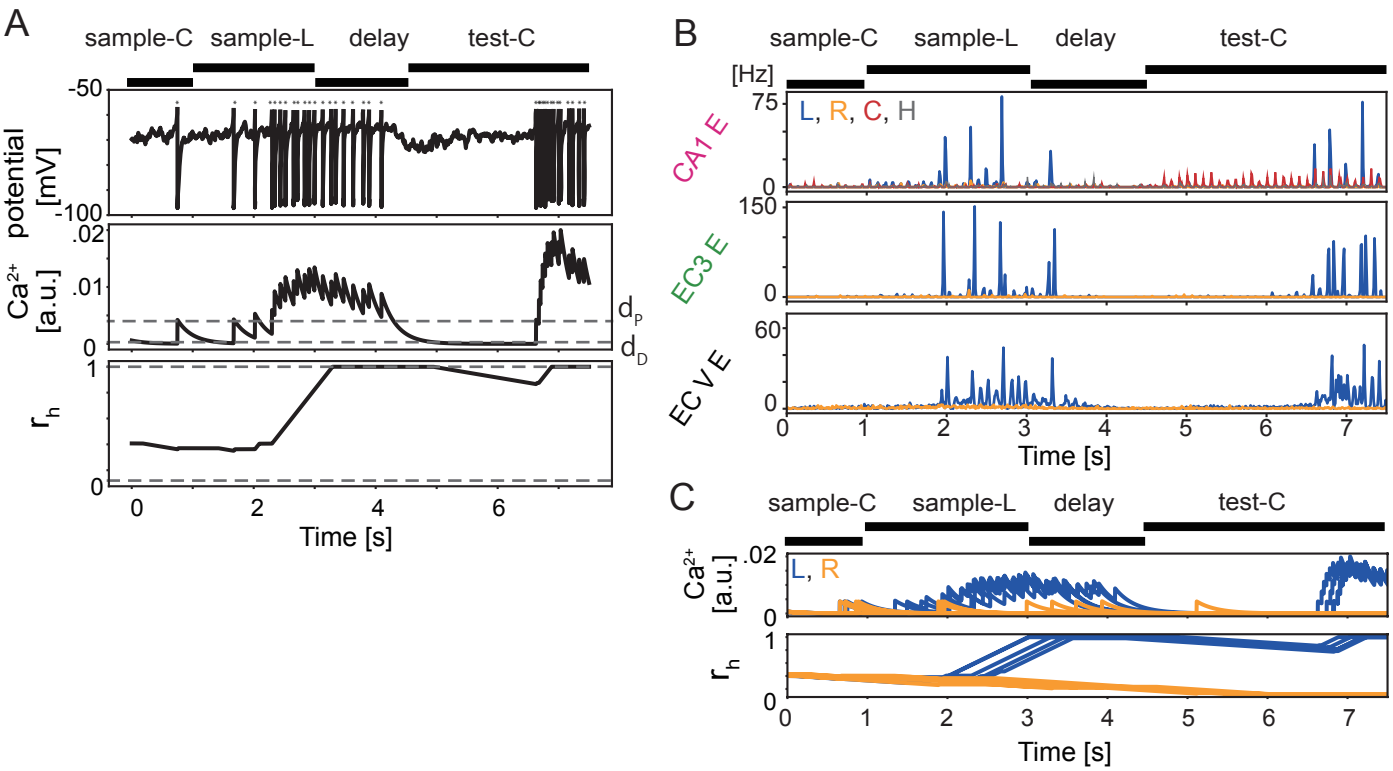
A
sample-C
sample-L
delay
test-C
potential [mV]
-50
-100
Ca2+ [a.u.]
.02
.01
0
dP
dD
rh
1
0
0
2
4
6
Time [s]
B
sample-C
sample-L
delay
test-C
[Hz]
CA1 E
75
0
L, R, C, H
EC3 E
150
0
EC V E
60
0
0
1
2
3
4
5
6
7
Time [s]
C
sample-C
sample-L
delay
test-C
Ca2+ [a.u.]
.02
0
L, R
rh
1
0
0
1
2
3
4
5
6
7
Time [s]

Figure 5. Role of CAN current in memory encoding and maintenance. (A) Single trial evolution of the membrane potential (top), [Ca^{2+}] (middle) and the ratio of high conductance state of CAN channels r_h (bottom) are plotted in an MECV excitatory (E) neuron. Dots above the membrane potential represent spikes. Broken lines denote two threshold values, dP and dD, in the middle panel and the upper and lower critical values of the high conductance ratio in the bottom panel (See Materials and methods). (B) Firing rates are shown for E neurons in CA1, MECIII and MECV. Colors indicate different neuron subgroups. (C) Time evolution of [Ca^{2+}] (top) and r_h (bottom) are plotted for randomly-chosen five MECV E neurons belonging to L (blue) or R (orange) subgroup during the same trial as in B.

573 Nevertheless, the fraction of high conductance state remained high in the subgroup L (but not
574 in the subgroup R) of MECV E neurons (Figure 5C).
575
576 The CAN current plays a crucial role in the maintenance of working memory. To explain this,
577 we divided the test-C period into early and late periods: in the early period CA1 neurons were
578 selectively activated in the subgroup C but not in the subgroup L (and subgroup R); in the late
579 period they were strongly activated in the subgroup L (Figure 5B). During the test-C period,
580 [ACh] was again increased, so was the activity of CA1 E neurons through the disinhibition
581 mechanism. Although MECV neurons in both subgroups L and R received synaptic input from
582 the CA1 subgroup C, MECV neurons were selectively activated in the subgroup L because the
583 high conductance rate remained high in these neurons. The activity of the MECV subgroup L
584 neurons gradually increased in the early test-C period, and eventually became sufficiently
585 strong to activate MECIII subgroup L neurons. Accordingly, the test-C period entered the late
586 period and the spatial information stored in MECV could be decoded by CA1 neurons. The
587 onset time of the late period depends on the realization of neural networks and initial
588 conditions. Thus, the covert activation of CAN current enables the retrieval of persistent
589 activity in the MECV subgroup L neurons for the decoding of spatial information in the test-C
590 period.
591
592 **Comparison of MECIII neural activity between the model and experiment**
593 We compared the responses of our model with those of the mouse entorhinal-hippocampal
594 circuit. For this comparison, we analyzed E neuron activity in MECIII after dividing each of the
595 sample-L, delay and test-C periods into early and late portions, respectively. As in experiment
596 (Yamamoto et al. 2014), we first quantified the intensity of theta oscillation in these task

periods by computing periodicity index (Materials and methods). As shown in Figure 6A, this index was high during the late sample-L, early delay, and late test-C periods, but it was low during delay period (i.e., late delay and early test-C periods). Periodicity index exhibited similar task period-dependence in the model and experiment (c.f. Figure 6C and Figure S5 in (Yamamoto et al. 2014)).

We next analyzed how the blockade of MECIII-to-CA1 projection affects the behavior of our model in different task periods. In the experiment, this blockade significantly impaired working memory performance of the mouse. When MECIII-to-CA1 projection was blocked during the encoding epoch (sample-L period), MECIII activity and the firing rate difference between L and R subgroups were suppressed during both sample-L and the subsequent late test-C periods (Figure 6B, blue), meaning that decoding ability was impaired. When the blockade was during the recall epoch (late test-C, 5.5-7.5 s), the inter-subgroup difference was reduced and decoding ability was also impaired (green line in Figure 6B). In contrast, when the blockade was imposed during sample-C (3-4.5 s) or early test-C period (4.5-6 s), MECIII activity was not greatly affected (Figure S3). Figure 6C summarizes the resultant decoding ability of the model. In three of the four conditions (blockade in sample-C, early and late test-C), results were well consistent with experimental observations (c.f., Figure 7F in (Yamamoto et al. 2014)). In addition, our model predicts that the blockade in sample-L period significantly impairs working memory performance ($p=3.175\times10^{-10}$), suggesting that the CA1-MECV-MECIII loop circuit maintains neural activity in the MECIII and plays a pivotal role in the spatial working memory task. This prediction should be experimentally validated.

Experimental validation of period-dependent preferred theta phases

Figure 6

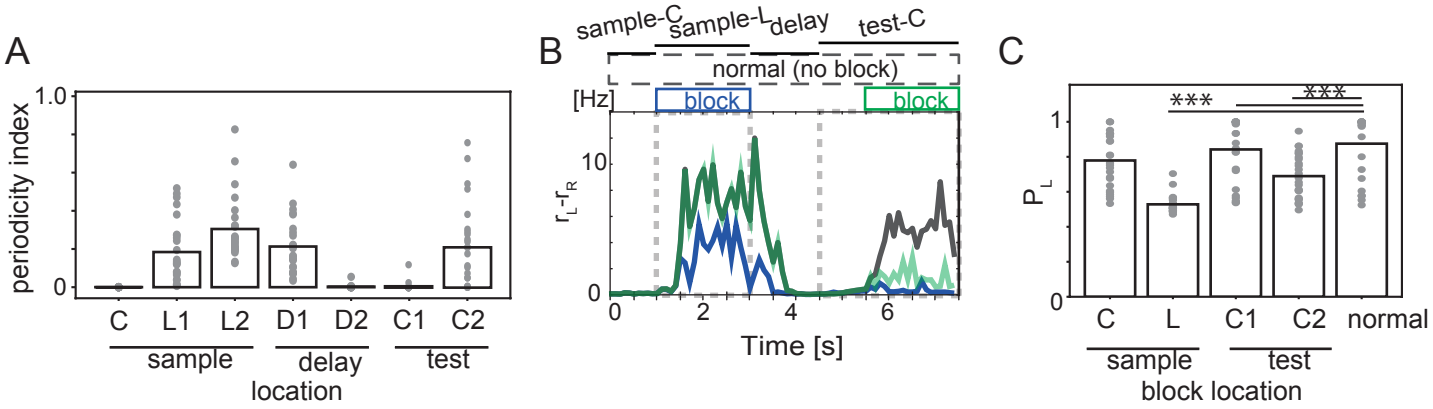
A
periodicity index
1.0
0
C
L1
L2
D1
D2
C1
C2
sample
delay
test
location
B
sample-C
sample-L
delay
test-C
normal (no block)
[Hz]
block
block
10
0
0
2
4
6
Time [s]
C
***
***
1
0
C
L
C1
C2
normal
sample
test
block location

Figure 6. Blockade of MECIII-to-CA1 connections during sample-L and late test-C periods. (A) Periodicity index (Yamamoto et al., 2014) was calculated for the activity of MECIII E neurons (Materials and methods). The labels L, D, C refer to sample-L, delay, test-C periods, respectively, and the numbers 1 and 2 label the early and late portions, respectively, of these periods. (B) Average differences in firing rate between the L and R subgroups of MECIII E neurons were calculated under the blockade of MECIII-to-CA1 connections: normal condition (black); the blockade during sample-L periods (blue); the blockade during late test-C periods (green). In each condition, the differences were averaged over five networks and five initial states. By definition, green and black lines overlap with one another before the blockade. Boxes above the traces indicate the periods of blockade. (C) P_L were calculated for different periods of the blockade.

621 Our model predicts that CA1 E neurons shift their preferred theta phases from the troughs to
622 the peaks when [ACh] is high (Figures 3B and 3E). In Figure 7A, we present the phase
623 preference of CA1 E neurons during sample-C, sample-L, delay, early test-center (test-C1) and
624 late test-center (test-C2) periods of the DNMP task. Their spikes preferred the troughs of theta
625 oscillation during sample-C periods but, owing to the disinhibitory mechanism, the preferred
626 phase was shifted to the peaks during sample-L periods. When the model mouse returned to
627 the home position (delay period), [ACh] was decreased to reactivate PV neurons in CA1, which
628 reduced the sensitivity of CA1 to inputs from MECIII and CA3 and selectively suppressed spike
629 generation at the peaks of theta oscillation (but not at the troughs). In test-C1 periods, [ACh]
630 was again increased to allow the activation of CAN current (Figure 5C), which shifted the
631 preferred phase to the descending phase of theta oscillation. During test-C2 periods, our
632 model predicts a progressive advance of preferred theta phase in CA1 due to an enhanced
633 synaptic drive by MECIII.
634
635 We confirmed these predictions in the data of a DNMP task in T-maze (Yamamoto et al. 2014).
636 Figure 7B shows the distributions of preferred phases of spikes in mouse CA1 during different
637 task periods, i.e., sample-C, sample-L (corresponding to the reward arm), delay, test-C1, and
638 test-C2 periods (see Materials and methods). In mice, spikes were generally not modulated by
639 theta oscillation as strongly as in the model. In particular, oscillatory modulations were weak
640 in sample-C periods. Nonetheless, the preferred theta phases in the various task periods are
641 well consistent between mice and models. The average preferred phase, which was computed
642 as $\bar{\theta} = \arg\left(\Sigma_{\mathrm{k}} \exp(i\theta_k)\right)$ with k being the index of spikes for all neurons and i being
643 imaginary unit, is delayed during delay periods compared to other task periods in both mice
644 and models (Figure 7C). In contrast, our model predicts that the preferred phase is

Figure 7

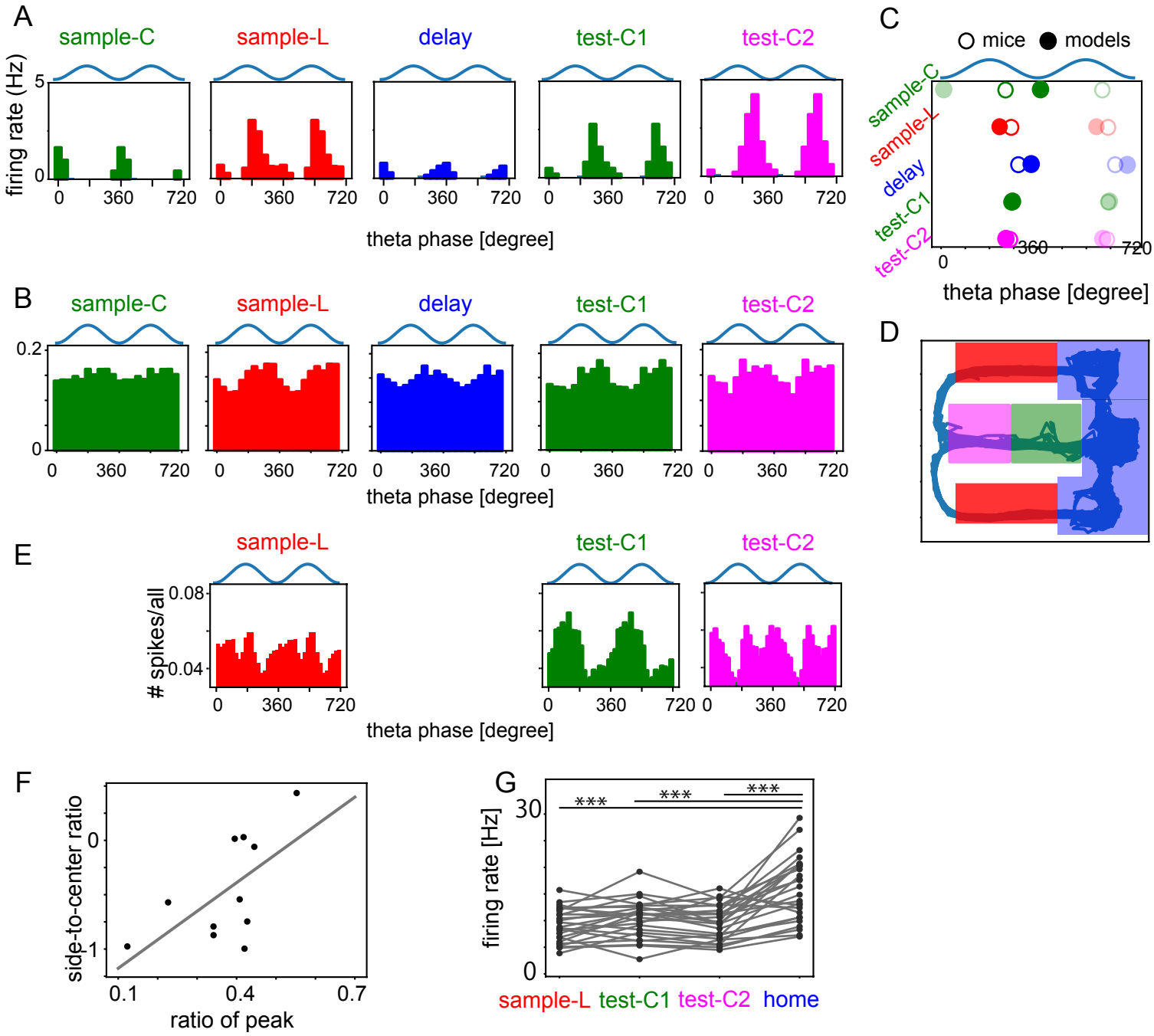
A
sample-C
sample-L
delay
test-C1
test-C2
firing rate (Hz)
5
0
0
360
720
theta phase [degree]
B
0.2
0
C
mice
models
sample-C
sample-L
delay
test-C1
test-C2
D
E
spikes/all
0.08
0.04
F
side-to-center ratio
0
-1
0.1
0.4
0.7
ratio of peak
G
firing rate [Hz]
30
***
sample-L
test-C1
test-C2
home

Figure 7. Preferred theta phases in model networks and rodents. (A) Phase preferences are shown for CA1 E neurons in model networks during given task periods (top). (B) Phase preference curves of CA1 neurons were calculated for data obtained in (Yamamoto et al., 2014). (C) Preferred theta phases of the models (filled circles) and mice (empty circles) were averaged over multiple theta cycles during given task periods. The same average phases are shown for two theta cycles (one in darker colors and one in light colors) for the clarity of the plots. (D) Schematic illustration of the figure-eight maze used in (Fernández-Ruiz et al., 2017; Mizuseki et al., 2013), which are also used in (E-G). Colored rectangles indicate early-center, late-center, and reward periods from which data were resampled. (E) Phase preference curves of CA1 excitatory neurons were calculated. For comparison, we divided the task periods of center arm and reward arm into early and late epochs. (F) Correlation between the ratios of spikes at the peaks and the side-to-center ratio is plotted. (G) The firing rates of PV neurons are plotted for different epochs. Each line represents a PV neuron. The firing rates in the home (indicated by blue area in D) is significantly higher than those in the sample-L, test-C1, and test-C2 epochs ($p=1.92\times10^{-7}$, 3.26×10^{-6}, 6.52×10^{-6}, respectively, *t* test on two related samples). We used PV neurons showing a sufficiently high firing rate (>5 Hz) during run (>1cm/s) across eight sessions.

progressively advanced during test-C2 (i.e., late test-center) period due to an increased synaptic drive by MECIII (Figure 5B).

Next, we asked whether preferred theta phase behaves similarly in an alternating figure-eight task (Mizuseki et al. 2013). We were particularly interested in examining the hypothesized role of cholinergic control of working memory function. In the alternating figure-eight task, rats were trained to alternately change the turn direction at a junction point of an eight-shape maze, meaning that the rats had to remember the turn direction of the preceding run. This task is similar to the previous DNMP task, but one difference is that sample and test trials are not clearly separated in the alternating figure-eight task. Nevertheless, we may correlate the behavioral epochs of the two tasks to each other. When rats traverse the center arm, they had to retrieve memory of the preceding choice to prepare for the next choice. Therefore, traveling along the center arm may correspond to test-C period in the DNMP task. Then, we can define three distinct areas on the eight-shape maze (Figure 7D): early center, late center and reward arms, which may correspond to test-C1, test-C2 and sample-L periods, respectively. Below, we follow these rules.

Figure 7E shows the preferred phases of excitatory neurons in the deep layer of CA1. It has been reported that for some unknown reason these neurons only exhibit phase shifts in early trials (Mizuseki et al. 2013; Fernández-Ruiz et al. 2017). Therefore, we only used data of initial ten trials in the following analyses. On the early center arm (test-C1 period), neurons fired more frequently around the troughs of theta oscillation than the peaks. However, on the late center arm (test-C2 period), neurons fired slightly more often at the peaks, generating two peaks per theta cycle in the spike density distribution. On the reward arm (sample-L period),

669 neurons fired most frequently at the peaks, which is consistent with the previous
670 study(Fernández-Ruiz et al. 2017). These results seem to be consistent with the model's
671 prediction that the preferred firing phase of CA1 neurons changes from the troughs to the
672 peaks of theta oscillation during the epochs of high [ACh]: in the alternating figure-eight task,
673 high level of attention, or high [ACh], is likely to be required on the reward arm (for encoding
674 reward information) and the late center arm (for recalling the previous choice).
675
676 Finally, we explored single-cell-level behavior in (Mizuseki et al. 2013) to provide further
677 support for our prediction: cells spiking on the side arms (cells in L or R subgroup in the model)
678 are likely to spike on the late center arm at the peaks of theta oscillation. Therefore, we
679 computed two ratios for 11 cells which showed high activation on the late center arm (See
680 Materials and methods for details): the number ratio of spikes generated around the peaks
681 (90° to 270°) to spikes generated on the late center arm; the number ratio of spikes generated
682 on the side arms to spikes generated on the late center arm (side-to-center ratio). The values
683 of the two ratios are significantly correlated (Figure 7F: r=0.62 and p=0.042, *t* test on two
684 related samples), suggesting that cells strongly activated on the side arms are also highly likely
685 to fire around the theta peaks. This result strongly supports the prediction of our model.
686
687 Our hypothesis predicted that the firing rate of PV neurons reduces during encoding (sample)
688 and recall (test-C1, C2) epochs but increases during the other epochs (home shown as the blue
689 area in the Figure7D) owing to [ACh] modulation. We examined the changes in the firing rate
690 of PV neurons at different epochs. We identified PV neurons in the previously recorded data
691 (Mizuseki et al. 2013) according to the criteria on the burst index and the refractory period
692 (Royer et al. 2012; Iwase et al. 2020) and measured the averaged firing rates of individual PV

neurons during the sample-L, test-C1, test-C2, and home epochs. As our model predicted, the firing rates of PV neurons were significantly higher in the resting epoch comparing to the other epochs (Figure 7G). These results strongly support our model.

Decoding performance depends on acetylcholine concentrations in the model

In our model, two ACh-regulated mechanisms, that is, disinhibitory circuit in CA1 and CAN current in MECV excitatory cells, play crucial roles in encoding, maintenance and recall epochs of working memory tasks. Therefore, we examined whether these core mechanisms work robustly when [ACh] is changed. We changed the default levels of [ACh] with other parameter values unchanged. Lowering the default [ACh], which weakens disinhibition, during the encoding epoch (sample-L) disenabled the CA1 L and R subgroups to exhibit large enough activity differences to encode spatial information in the CA1-MECV-MECIII loop circuit (Figure 8A, blue). Decoding performance was severely impaired, contrasting to intact performance at higher default [ACh] levels (Figure 8B, left). Lower default [ACh] levels during delay period had almost no effects on decoding ability (Figure 8B, center). Finally, lower default [ACh] levels during the recall epoch (test-C2) eliminated the reactivation of the subgroup L (Figure 8A, green) and decoding ability was severely impaired (Figure 8B, right), but performance remained intact at higher [ACh] levels. These results show that default [ACh] levels should be sufficiently high during the encoding and recall epochs, but fine tuning of [ACh] is unnecessary.

Next, we explored whether theta-phase-locked firing has anything to do with the success of the working memory task. To this end, we compared the theta preference of CA1 neurons during the test-C2 period between successful and failure trials in both models and mice (Figure 8C). [ACh] was at the default levels. In both models and mice, neurons preferentially fired

Figure 8

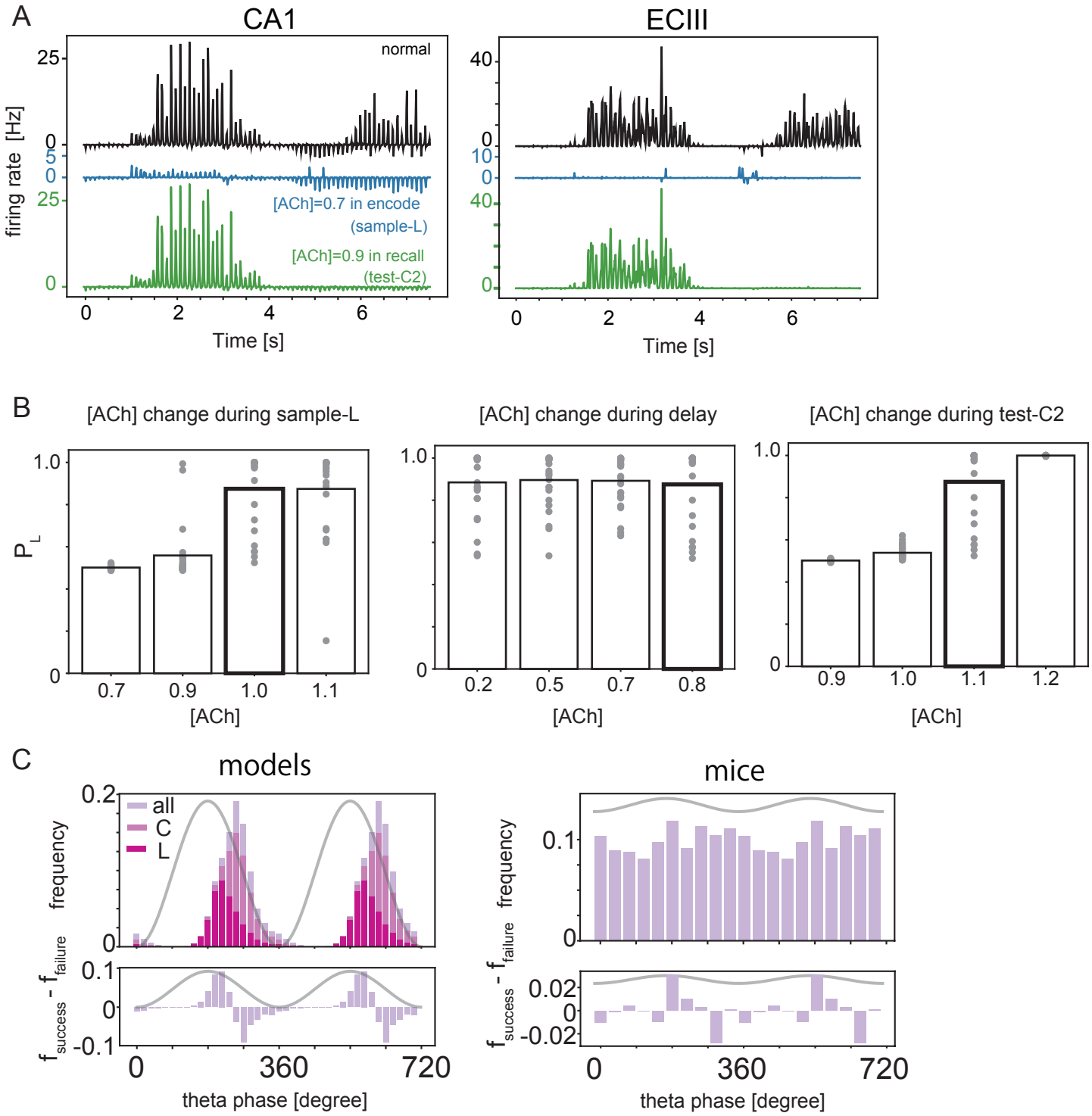
A
CA1
ECIII
normal
[ACh]=0.7 in encode
(sample-L)
[ACh]=0.9 in recall
(test-C2)
firing rate [Hz]
Time [s]
B
[ACh] change during sample-L
[ACh] change during delay
[ACh] change during test-C2
P_L
[ACh]
C
models
mice
all
C
L
frequency
f_success - f_failure
theta phase [degree]

Figure 8. Cholinergic modulations in the network model. (A) In CA1 (left) and MECIII (right), differences in firing rate between the subgroups L and R were calculated at the normal (black) and reduced levels of [ACh] during encoding (sample-C, blue) and recall (test-C2, green) epochs. (B) Probability of left choice averaged over different networks and initial conditions are shown at different levels of [ACh] during sample-L (left), delay (center) and test-C2 (right) periods. Thick lines indicate results for the default [ACh] levels. (C) Frequency of spikes in CA1 excitatory neurons during test-C2 periods (top) are shown in the model (left) and mice (right). In the model, [ACh] was set to the normal level and spike counts are shown separately for the subgroups L and C. Only the total spike count is shown for mice. Bottom panels show the differences in firing rate between successful and failure trials.

around the peaks of theta oscillation in success trails, but firing phases were somewhat delayed in failure trials.

Role of high-gamma oscillation in memory processing in MECIII and CA1

Decision making in mice was accompanied by a rapid increase in coherent high-gamma oscillations (60 -120 Hz) between MECIII and CA1 (Yamamoto et al. 2014). However, we did not model the mechanism to generate prominent gamma oscillations to keep our model mathematically simple and minimal. Actually, the simplified mathematical description was sufficient for accounting for many findings on neural activity and mouse behavior reported in the experiment. Then, the question arises about the role of coherent high gamma oscillation in the working memory task. To answer this question, we applied a common oscillatory input in the high-gamma range (80 Hz) to E neurons in MECIII and CA1 (Figure 9A: also see the Materials and Methods). In the experiment, high gamma oscillations of LFPs were synchronized between MECIII and the lacunosum molecule layer of CA1, to which MECIII-to-CA1 connections project, indicating a common source of high gamma oscillations projecting to both areas.

High gamma oscillation improved the decoding of memorized information from the entorhinal-hippocampal loop circuit in the model. To show this, we built a virtual decoder of excitatory and inhibitory neurons receiving inputs from MECIII and CA1 (Figure 9A, see the STAR method for details), because feedforward inhibition is a ubiquitously found motif of cortico-cortical synaptic connections (Isaacson and Scanziani 2011). Stimulated by the high gamma input, E neurons in both areas tended to fire in the high-gamma frequency range (Figure 9B). Spike bursts were delayed in CA1 by about 10 ms from those in MECIII, which is

Figure 9

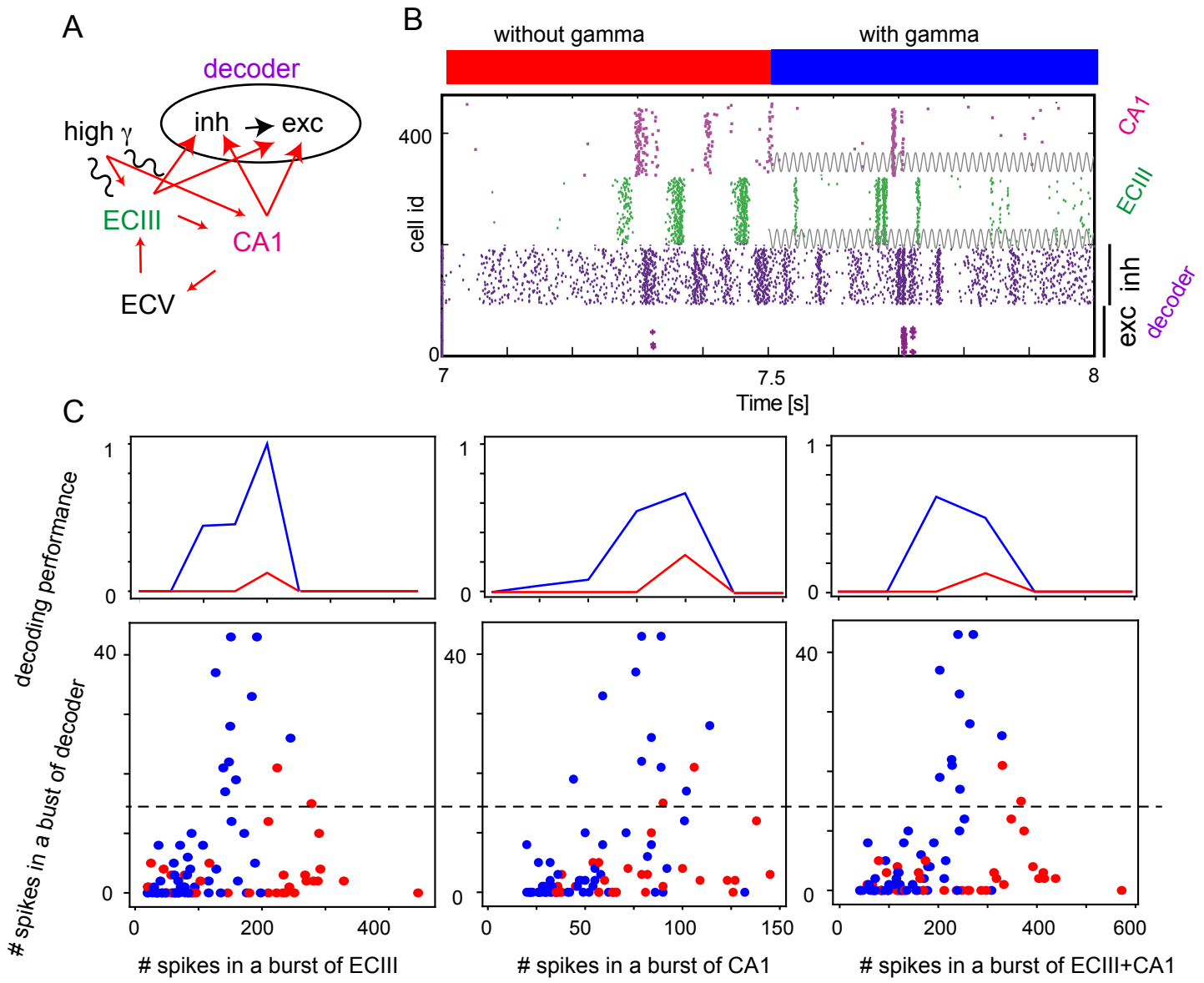
A
decoder
high γ
inh
exc
ECIII
CA1
ECV
B
without gamma
with gamma
400
cell id
0
7
7.5
8
Time [s]
CA1
ECIII
inh
exc
decoder
C
decoding performance
1
0
spikes in a bust of decoder
40
0
200
400
spikes in a burst of ECIII
50
100
150
spikes in a burst of CA1
600
spikes in a burst of ECIII+CA1

Figure 9. Role of high-gamma oscillation in information decoding. (A) Decoding of choice information from MECIII and CA1 is schematically illustrated. (B) Raster plots are shown for CA1 and MECIII E neurons in the subgroup L and excitatory and inhibitory neurons in the decoder. From 7.5 [s] to 8 [s], a common coherent high-gamma input was applied to MECIII E and CA1 E neurons. (C) Decoder performance (upper) and the number of spikes of excitatory decoder neurons (bottom) evoked by a single burst in MECIII (left), CA1 (middle) or both (right) are plotted. Spike counts obtained with (blue) and without (red) the high-gamma oscillatory input are displayed. The decoder performance was defined as the probability that the number of output spikes in a burst exceeds a threshold value (dotted lines in bottom panels) for a given input burst size.

consistent with experimental observation (Yamamoto et al. 2014). Because this delay is approximately equal to the period of high gamma oscillation, synaptic inputs from the two areas coincidently arrived at the decoder in each high-gamma cycle. The coincident input amplified the evoked responses and facilitated spike firing of the decoder. In contrast, without the high gamma input, inputs from MECIII and CA1 did not arrive coherently to the decoder. Actually, successive activations of CA1 and MECIII without high-gamma stimulation around 7.3 sec in Figure 9B do not evoke strong activation in decoder neurons, while those of CA1 and MECIII around 7.7 sec evoke a burst of decoder neurons. Feedforward inhibition further attenuated the impact of incoherent spike input on decoder neurons. Thus, coherent high gamma activity in MECIII and CA1 may facilitate the readout of spatial information from MECIII by other cortical areas.

To generalize this observation, in Figure 9C, we quantified decoder performance while changing burst size (the number of spikes per burst) in MECIII and CA1. The performance was measured by the probability that coincident bursts in CA1 and MECIII generate a spike burst in a decoder neuron. Without gamma oscillation, even a large burst in MECIII and/or CA1 could not evoke a burst in the decoder. In contrast, in the presence of gamma oscillation a small burst in MECIII and/or CA1 was sufficient for evoking a burst in the decoder with high fidelity. These results further support the role of coherent high gamma oscillation in facilitating the decoder performance. It is noted that an increased high gamma coherence between CA1 and MECIII enhanced the performance even if the input burst size was reduced.

Discussion

765

766 In this study, we developed a model comprising MECV, MECIII and CA1 to explore how these
767 local circuits process and communicate information with each other regulated by ACh during
768 DNMP tasks. In our model, changes in the ACh concentration control cortical disinhibitory
769 systems and calcium-dependent cationic current to perform different cognitive functions in
770 DNMP tasks. With the ACh modulations, our model successfully replicates the various features
771 of neural activity observed in MECIII and CA1 (Yamamoto et al. 2014). In particular, the model
772 predicts that CA1 neurons change their preferred theta phases depending on cognitive
773 demands, which was also supported by experimental data (Mizuseki et al. 2013; Yamamoto
774 et al. 2014; Fernández-Ruiz et al. 2017).

775

776 **Relevance of MEC-CA1 loop to spatial working memory tasks**

777 The hippocampal area CA1 is a central locus for spatial information processing, and stores the
778 concurrent position of the rodent (O'Keefe and Dostrovsky 1971) as well as retrospective and
779 prospective representations of position information (Ferbinteanu et al. 2003; Dragoi and
780 Buzsáki 2006; Foster and Wilson 2006; Pastalkova et al. 2008; Gupta et al. 2010; Zheng et al.
781 2016). Focusing on the CA1-MECV-MECIII loop circuit involved in spatial working memory
782 (Witter et al. 2000; van Strien et al. 2009), we demonstrated how the spatial information of
783 the selected arm is encoded in CA1 during a sample trial (Figure 4), maintained in MECV during
784 delay period, and transferred to MECIII and reloaded on CA1 for decision making (Figure 5).
785 Several studies found that connections from MECIII to CA1 are crucial for the success of spatial
786 working memory tasks (Suh et al. 2011; Yamamoto et al. 2014). Our model demonstrated this
787 role of MECIII-to-CA1 connections in spatial working memory, predicting their crucial

788 contribution to memory encoding by the entorhinal-hippocampal loop circuit. The predicted
789 operation of the loop circuit should be tested experimentally.
790
791 Sequence of spikes with theta phase precession, that is, “theta sequence” (Ferbinteanu et al.
792 2003; Pfeiffer and Foster 2013; Schlesiger et al. 2015; Middleton and McHugh 2016; Zheng et
793 al. 2016), has been observed in the hippocampus and the MEC during cognitive tasks requiring
794 episodic memory. The blockade of MECIII-to-CA1 connections causes modulation of theta
795 activity in MECIII (Suh et al. 2011; Yamamoto et al. 2014). Similarly, inactivation of the MEC
796 disrupts the temporal organization of spikes and impairs information maintenance (Robinson
797 et al. 2017). These results imply that the temporal coordination of theta-phase-locked
798 neuronal firing along the CA1-MECV-MECIII loop circuit is crucial for the success of spatial
799 working memory tasks. We showed an example case in which the disruption of this temporal
800 coordination in MECIII led to a significant increase of failure trials (Figure 3A, B).
801
802 Our model assumes that [ACh] changes in time during a working memory task and predicts
803 that these changes shift the preferred theta phase in CA1 E neurons: higher [ACh] advances
804 the preferred phase towards the peak of theta oscillation (Figure 7). Specifically, the model
805 predicts that phase advances occur during the encoding epoch in sample trials (i.e., on the
806 reward arm) and during the recall epoch in test trials (i.e., on the center arm). We validated
807 this prediction with the results of two experiments (Mizuseki et al. 2013; Yamamoto et al.
808 2014; Fernández-Ruiz et al. 2017). Phase advances in the encoding epoch have been known
809 previously and can be accounted for by temporal separation between CA3 input and MECIII
810 input to CA1 (Hasselmo et al. 2002; Colgin et al. 2009; Cutsuridis et al. 2010; Milstein et al.
811 2015; Lasztóczi and Klausberger 2016). Input from CA3 preferentially arrives at CA1 on the

descending phase of theta oscillation of LFP (Klausberger and Somogyi 2008) whereas input from MECIII arrives at the peaks of theta oscillation (Hasselmo et al. 2002; Mizuseki et al. 2009; Fernández-Ruiz et al. 2017). Because MECIII input, which presumably carries sensory information, seems to dominate CA3 input during encoding (Hasselmo2002), CA1 neurons likely fire at the peaks rather than the troughs of theta oscillation (Fernández-Ruiz et al. 2017).

Phase advances on the later central arm (i.e., in the recall epoch) represent a novel finding of this study. CA1 neurons were previously shown to fire at the troughs of theta oscillation during memory recall (Fernández-Ruiz et al. 2017), and this was consistent with the view that CA3 input dominates MECIII input during this epoch. Challenging the conventional view, our model predicts that CA1 neurons retrieve spatial memory from the MECIII, hence firing at the peaks of theta oscillation. Possibly consistent with this prediction, if we divide the center arm into early and late portions in (Mizuseki et al. 2009), preferred theta phases show a second (and advanced) peak in the late portion of recall epoch (Figure 7D). This peak was absent in the previous analysis (Fernández-Ruiz et al. 2017) because the center arm was treated as a single entity. The consistency between the model and experiment requires further clarification.

Reflection of cognitive demands on the MEC-CA1 loop circuit through ACh

ACh is involved with several cognitive functions such as sensory discrimination (Pinto et al. 2013; Hangya et al. 2015), associative learning (Sabec et al. 2018), and spatial (Croxson et al. 2011; Okada et al. 2015) and non-spatial working memory (Furey et al. 2000; McGaughy et al. 2005; Hasselmo and Stern 2006). In correlation with cognitive states, ACh concentration changes to modulate activity of the specific types of neurons (Womelsdorf et al. 2014; Muñoz et al. 2017) through muscarinic and nicotinic receptors (Parikh et al. 2007; Zhang et al. 2010;

836 Teles-Grilo Ruivo et al. 2017). In associative learning, ACh was suggested to facilitate MECIII-
837 to-CA1 input during the encoding epoch and CA3-to-CA1 input during the decoding epoch
838 (Hasselmo 2006). We propose a novel role and mechanism of ACh for the functions of the
839 entorhinal-hippocampal loop circuit according to the cognitive demands arising during a
840 spatial working memory task, namely, memory encoding, maintenance and recall. Consistent
841 with the proposal of our model (Figure 2B), it has recently been shown in a DNMP task (Teles-
842 Grilo Ruivo et al. 2017) that [ACh] is significantly higher on the reward arm than in other
843 positions in both sample and test trials, that on the center arm [ACh] tends to be larger in test
844 trials than in sample trials, and that [ACh] is low in delay periods (c.f., Figure 8B).
845
846 We assumed that a change in cognitive demands is reflected in a phasic change in [ACh] on
847 the timescale of seconds. However, [ACh] is thought to change in a diffusive and tonic manner
848 on much slower timescales of minutes or hours. Importantly, recent studies have revealed
849 that [ACh] undergoes phasic changes at sub-second and second timescales (Parikh et al. 2007;
850 Zhang et al. 2010; Teles-Grilo Ruivo et al. 2017), and such a phasic change in [ACh] is associated
851 with reward or aversive signals (Hangya et al. 2015). Further, task performance is correlated
852 with slower tonic increases in [ACh] during the task period (Parikh et al. 2007), but
853 uncorrelated with phasic changes in [ACh] in the reward arm (Teles-Grilo Ruivo et al. 2017). In
854 our model, task performance saturates above a certain level of [ACh] in the reward arm (Left
855 panel in Figure 8B). Our results suggest that the tonic level of [ACh] expresses an overall bias
856 during each trial and a phasic increase in [ACh] gives a more elaborate modulation reflecting
857 a specific cognitive demand.
858
859 **Dynamic processing across multiple areas**

Coherence in neural activity between different cortical areas varies with the cognitive state of the brain (Benchenane et al. 2010; Fries 2015). Furthermore, disruption of a cortico-cortical interaction at different behavioral states can impair task performance differently (Yamamoto et al. 2014; Spellman et al. 2015). These results imply that information flows between cortical areas are differentially routed according to the demand of the on-going cognitive process through the dynamical regulation of corticocortical coherence. Theoretical studies have proposed several mechanisms of information routing based on a balance control between excitatory and inhibitory synaptic inputs (Vogels and Abbott 2009), disinhibitory circuits (Yang et al. 2016), spontaneous bursts (Palmigiano et al. 2017), and band-pass filtering by a feed-forward inhibitory circuit (Akam and Kullmann 2010). While these studies focused on the circuit mechanisms of information routing, we addressed how such mechanisms are integrated to perform a spatial working memory task through different cognitive demands (Benchenane et al. 2010; Yamamoto et al. 2014; Spellman et al. 2015). We demonstrated that cholinergic inputs coordinate the encoding and recall functions by modulating the cortical disinhibitory circuit and Ca^{2+}-dependent cationic channels in excitatory cells.

Accumulating evidence suggests that disinhibitory circuits play a crucial role in various cognitive tasks such as fear conditioning (Letzkus et al. 2011; Pi et al. 2013) and sensory discrimination (Pinto et al. 2013; Hangya et al. 2015). The dominant interneuron types of the disinhibitory circuits are VIP, SOM and PV inhibitory neurons (Donato et al. 2013; Zhang et al. 2014; Kamigaki and Dan 2017; Francavilla et al. 2018). Among these neurons, VIP neurons express muscarinic receptors and are depolarized by cholinergic input (Bell et al. 2015) and are thought to project more strongly to SOM neurons than to PV neurons in cortical areas (Zhang et al. 2014; Kamigaki and Dan 2017). However, some studies suggest stronger

884 cholinergic modulations of PV neurons in the hippocampus (Donato et al. 2013; Francavilla et
885 al. 2018). As explained below, the cholinergic modulation of OLM neurons also does not
886 strongly influence the firing of CA1 E neurons. Therefore, in this study we mainly analyzed the
887 effect of PV neurons on neural circuit functions. In line with our model's prediction (Figure S2),
888 optogenetic inhibition of PV neurons impairs performance in spatial working memory (Murray
889 et al. 2011).
890
891 PV neurons preferentially fire in the descending phase of theta oscillation (Klausberger and
892 Somogyi 2008) to weaken the effect of CA3-to-CA1 input. In contrast, SOM (OLM in CA1)
893 neurons preferably spike at the troughs of theta oscillation (Klausberger and Somogyi 2008;
894 Royer et al. 2012) much earlier than the CA3 input. In our model, excitatory MECIII input
895 innervates CA1 preferentially at the theta peaks but rarely at the theta troughs. Therefore,
896 the ACh-induced suppression of OLM neurons does not also enhance the effect of MECIII input
897 on excitatory neuron firing in CA1, making OLM neurons less effective than PV neurons in
898 modulating the CA1 activity. In rats, however, the actual spikes delivered by the MECIII are
899 distributed broadly over a theta cycle (Mizuseki et al. 2009), implying that the suppression of
900 PV and SOM neurons can induce a complex modulatory effect in CA1 pyramidal neurons. Our
901 model predicts that the inactivation of PV or VIP neurons (in this case both PV and SOM are
902 released from the inhibition by VIP neurons) impairs decoding ability in different ways (Figure
903 S2). This prediction needs to be confirmed by experiments.
904
905 **Covert memory state for maintenance of information**
906 Recent studies showed that dynamically evolving neuronal activity can maintain information
907 during a delay period in working memory tasks (Stokes 2015; Murray et al. 2017; Wolff et al.

908 2017). In the DNMP task we studied (Yamamoto et al. 2014), theta phase-locked firing of
909 MECIII neurons was correlated with the success of the task. Nevertheless, this neuronal
910 activity temporarily vanished during a delay period, implying that a non-spiking activity
911 maintains information on the previous choice. We hypothesized that the conductance of a
912 specific ionic channel, i.e., calcium-dependent cationic current, remains in an elevated state
913 to preserve spatial information during delay period. This elevated state is not accompanied by
914 neuronal firing, hence is consistent with experimental observations. This mechanism was
915 originally proposed to account for persistent activity of isolated single neurons (Fransen et al.
916 2002; Fransén et al. 2006) and suggested to be engaged in temporal association memory
917 (Kitamura et al. 2014). Our model demonstrates that the same mechanism can generate a
918 covert memory state necessary in spatial working memory. This and other mechanisms of
919 covert memory state, for instance, short-term synaptic plasticity (Mongillo et al. 2008), are
920 not mutually exclusive. However, our mechanism has an important advantage that working
921 memory maintenance is turned on and off by cholinergic modulation depending on the
922 cognitive demand. Thus, our results suggest that neuromodulators are crucial for the flexible
923 control of memory processing by the brain.
924
925 **Limitation of the model**
926 We showed that coherent activations of CA1 and MECIII at high-gamma frequencies facilitate
927 decoding of information about the previous choice from CA1 and MECIII (Figure 9). However,
928 gamma oscillation is not absolutely necessary in our model for performing spatial working
929 memory tasks. Theta-phase-locked neuronal firing alone could sufficiently facilitate
930 information transfer along the MECIII-CA1-MECV loop circuit without gamma oscillation. This
931 result may somewhat contradict the experimentally suggested role of gamma oscillation in

information transfer between the hippocampus and entorhinal cortex (Colgin et al. 2009; Yamamoto et al. 2014). The role of gamma oscillation needs to be further explored.

Secondly, we did not model any mechanism to translate the decoded information into a correct choice behavior under a given rule of decision making (e.g., the alternative of left or right turn). The mPFC is projected to by CA1 and projects back to it via reuniens (Dolleman-Van Der Weel and Witter 1996; Ito et al. 2015), and is engaged in spatial working memory (Jones and Wilson 2005; Spellman et al. 2015; Bolkan et al. 2018). Furthermore, some mPFC neurons exhibit rule-related activities. However, the delay-period activity of mPFC neurons is specific to neither previous nor present location in a DNMP task (Bolkan2017) and the rule-related activities are not location-specific (Durstewitz et al. 2010; Preston and Eichenbaum 2013; Guise and Shapiro 2017). Where and how decision rules are processed and how spatial working memory and rule-related activities are integrated are open to future studies.

Acknowledgement

We thank Jun Yamamoto for providing experimental data and fruitful discussion, Motosada Iwase for advice in data analysis, and György Buzsáki for publicly sharing the valuable data. This work was supported by KAKENHI (nos. 18H05213, 18K15343 and 19H04994) from the MEXT, Japan.

Data and Software Availability

The computer codes used to generate the present simulation results will be available upon request.

Declaration of Interests

The authors declare no competing interests.

References

Akam TE, Kullmann DM. 2010. Oscillations and Filtering Networks Support Flexible Routing of Information. Neuron. 67:308–320.

Albuquerque EX, Pereira EFR, Alkondon M, Rogers SW. 2009. Mammalian Nicotinic Acetylcholine Receptors: From Structure to Function. Physiol Rev. 89:73–120.

Bell LA, Bell KA, Mcquiston AR. 2015. Activation of muscarinic receptors by ACh release in hippocampal CA1 depolarizes VIP but has varying effects on parvalbumin-expressing basket cells. J Physiol. 1:197–215.

968 Benchenane K, Peyrache A, Khamassi M, Tierney PL, Gioanni Y, Battaglia FP, Wiener SI. 2010.
969 Coherent Theta Oscillations and Reorganization of Spike Timing in the Hippocampal-
970 Prefrontal Network upon Learning. Neuron. 66:921–936.
971 Bittner KC, Grienberger C, Vaidya SP, Milstein AD, Macklin JJ, Suh J, Tonegawa S, Magee JC.
972 2015. Conjunctive input processing drives feature selectivity in hippocampal CA1
973 neurons. Nat Neurosci. 18:1–13.
974 Bolkan SS, Stujenske JM, Parnaudeau S, Spellman TJ, Rauffenbart C, Abbas AI, Harris AZ,
975 Gordon JA, Kellendonk C. 2018. Thalamic projections sustain prefrontal activity during
976 working memory maintenance. Nat Neurosci. 20:987–996.
977 Borhegyi Z, Varga V, Freund F. 2004. Phase Segregation of Medial Septal GABAergic Neurons
978 during Hippocampal Theta Activity. J Neurosci. 24:8470–8479.
979 Buehlmann A, Deco G. 2010. Optimal Information Transfer in the Cortex through
980 Synchronization. PLoS Comput Biol. 6:e1000934.
981 Colgin LL, Denninger T, Fyhn M, Hafting T, Bonnevie T, Jensen O, Moser M-B, Moser EI. 2009.
982 Frequency of gamma oscillations routes flow of information in the hippocampus.
983 Nature. 462:353–357.
984 Croxson PL, Kyriazis DA, Baxter MG. 2011. Cholinergic modulation of a specific memory
985 function of prefrontal cortex. Nat Neurosci. 14:1510–1512.
986 Cutsuridis V, Cobb S, Graham BP. 2010. Encoding and retrieval in a model of the
987 hippocampal CA1 microcircuit. Hippocampus. 20:423–446.
988 Dolleman-Van Der Weel M, Witter MP. 1996. Projections From the Nucleus Reuniens
989 Thalami to the Entorhinal Cortex , Hippocampal Field CA1 , and the Subiculum in the Rat
990 Arise From Different Populations of Neurons. J Comp Neurol. 364:637–650.

991 Donato F, Rompani SB, Caroni P. 2013. Parvalbumin-expressing basket-cell network plasticity
992 induced by experience regulates adult learning. Nature. 504:272–276.
993 Dragoi G, Buzsáki G. 2006. Temporal Encoding of Place Sequences by Hippocampal Cell
994 Assemblies. Neuron. 50:145–157.
995 Durstewitz D, Vittoz NM, Floresco SB, Seamans JK. 2010. Abrupt transitions between
996 prefrontal neural ensemble states accompany behavioral transitions during rule
997 learning. Neuron. 66:438–448.
998 Egorov a V, Hamam BN, Fransen E, Hasselmo ME, Alonso AA. 2002. Graded persistent
999 activity in entorhinal cortex neurons. Nature. 420:173–178.
1000 Eichenbaum H. 2017. Prefrontal–hippocampal interactions in episodic memory. Nat Rev
1001 Neurosci. 18:547–558.
1002 Ferbinteanu J, Shapiro ML, Place GLL, York N, York N. 2003. Prospective and Retrospective
1003 Memory Coding in the Hippocampus. Neuron. 40:1227–1239.
1004 Fernández-Ruiz A, Oliva A, Nagy GA, Maurer AP, Berényi A, Buzsáki G. 2017. Entorhinal-CA3
1005 Dual-Input Control of Spike Timing in the Hippocampus by Theta-Gamma Coupling.
1006 Neuron. 93:1213-1226.e5.
1007 Foster DJ, Wilson MA. 2006. Reverse replay of behavioural sequences in hippocampal place
1008 cells during the awake state. Nature. 440:680–683.
1009 Francavilla R, Villette V, Luo X, Chamberland S, Muñoz-Pino E, Camiré O, Wagner K, Kis V,
1010 Somogyi P, Topolnik L. 2018. Connectivity and network state-dependent recruitment of
1011 long-range VIP-GABAergic neurons in the mouse hippocampus. Nat Commun. 9:5043.
1012 Fransen E, Alonso AA, Hasselmo ME. 2002. Simulations of the role of the muscarinic-
1013 activated calcium-sensitive nonspecific cation current INCM in entorhinal neuronal
1014 activity during delayed matching tasks. J Neurosci. 22:1081–1097.

1015 Fransén E, Tahvildari B, Egorov A V, Hasselmo ME, Alonso A a. 2006. Mechanism of graded
1016 persistent cellular activity of entorhinal cortex layer v neurons. Neuron. 49:735–746.
1017 Fries P. 2015. Rhythms for Cognition: Communication through Coherence. Neuron. 88:220–
1018 235.
1019 Furey ML, Pietrini P, Haxby J V. 2000. Cholinergic enhancement and increased selectivity of
1020 perceptual processing during working memory. Science (80-). 290:2315–2319.
1021 Gonzalez-Sulser A, Parthier D, Candela A, McClure C, Pastoll H, Garden D, Surmeli G, Nolan
1022 MF. 2014. GABAergic Projections from the Medial Septum Selectively Inhibit
1023 Interneurons in the Medial Entorhinal Cortex. J Neurosci. 34:16739–16743.
1024 Guise KG, Shapiro ML. 2017. Medial Prefrontal Cortex Reduces Memory Interference by
1025 Modifying Hippocampal Encoding. Neuron. 94:183-192.e8.
1026 Gupta AS, van der Meer MAA, Touretzky DS, Redish AD. 2010. Hippocampal Replay Is Not a
1027 Simple Function of Experience. Neuron. 65:695–705.
1028 Hangya B, Ranade SP, Lorenc M, Kepecs A. 2015. Central Cholinergic Neurons Are Rapidly
1029 Recruited by Reinforcement Feedback. Cell. 162:1155–1168.
1030 Hasselmo ME. 2006. The role of acetylcholine in learning and memory. Curr Opin Neurobiol.
1031 16:710–715.
1032 Hasselmo ME, Bodelón C, Wyble BP, Âon CB, Wyble BP, Hasselmo ME, Âon CB, Wyble BP.
1033 2002. A proposed function for hippocampal theta rhythm: Separate phases of encoding
1034 and retrieval enhance reversal of prior learning. Neural Comput. 14:793–817.
1035 Hasselmo ME, Sarter M. 2010. Modes and Models of Forebrain Cholinergic
1036 Neuromodulation of Cognition. Neuropsychopharmacology. 36:52–73.
1037 Hasselmo ME, Stern CE. 2006. Mechanisms underlying working memory for novel
1038 information. Trends Cogn Sci. 10:487–493.

1039 Isaacson JS, Scanziani M. 2011. How inhibition shapes cortical activity. Neuron. 72:231–243.
1040 Ito HT, Zhang S, Witter MP, Moser EI, Moser M. 2015. A prefrontal–thalamo–hippocampal
1041 circuit for goal-directed spatial navigation. Nature. 522:50–55.
1042 Iwase M, Kitanishi T, Mizuseki K. 2020. Cell type, sub-region, and layer-specific speed
1043 representation in the hippocampal–entorhinal circuit. Sci Rep. 10:1407.
1044 Jones MW, Wilson MA. 2005. Theta Rhythms Coordinate Hippocampal–Prefrontal
1045 Interactions in a Spatial Memory Task. PLoS Biol. 3:e402.
1046 Kamigaki T, Dan Y. 2017. Delay activity of specific prefrontal interneuron subtypes
1047 modulates memory-guided behavior. Nat Neurosci. 20:854–863.
1048 Kitamura T, Pignatelli M, Suh J, Kohara K, Yoshiki A, Abe K, Tonegawa S. 2014. Island Cells
1049 Control Temporal Association Memory. Science (80-). 343:896–901.
1050 Klausberger T, Somogyi P. 2008. Neuronal diversity and temporal dynamics: the unity of
1051 hippocampal circuit operations. Science (80-). 321:53–57.
1052 Lasztóczi B, Klausberger T. 2016. Hippocampal Place Cells Couple to Three Different Gamma
1053 Oscillations during Place Field Traversal. Neuron. 91:34–40.
1054 Letzkus JJ, Wolff SBE, Lüthi A. 2015. Disinhibition, a Circuit Mechanism for Associative
1055 Learning and Memory. Neuron. 88:264–276.
1056 Letzkus JJ, Wolff SBE, Meyer EMM, Tovote P, Courtin J, Herry C, Lüthi A. 2011. A disinhibitory
1057 microcircuit for associative fear learning in the auditory cortex. Nature. 480:331–335.
1058 McGaughy J, Koene RA, Eichenbaum H, Hasselmo ME. 2005. Cholinergic Deafferentation of
1059 the Entorhinal Cortex in Rats Impairs Encoding of Novel But Not Familiar Stimuli in a
1060 Delayed Nonmatch-to-Sample Task. J Neurosci. 25:10273–10281.
1061 Middleton S, Jalics J, Kispersky T, Lebeau FEN, Roopun AK, Kopell NJ, Whittington MA,
1062 Cunningham MO. 2008. NMDA receptor-dependent switching between different

1063 gamma rhythm-generating microcircuits in entorhinal cortex. Proc Natl Acad Sci U S A.
1064 105:18572–18577.
1065 Middleton SJ, McHugh TJ. 2016. Silencing CA3 disrupts temporal coding in the CA1
1066 ensemble. Nat Neurosci. 19:945–951.
1067 Milstein AD, Bloss EB, Apostolides PF, Vaidya SP, Dilly GA, Zemelman B V, Magee JC. 2015.
1068 Inhibitory Gating of Input Comparison in the CA1 Microcircuit. Neuron. 87:1274–1289.
1069 Mizuseki K, Diba K, Pastalkova E, Buzsáki G. 2011. Hippocampal CA1 pyramidal cells form
1070 functionally distinct sublayers. Nat Neurosci. 14:1174-.
1071 Mizuseki K, Sirota A, Pastalkova E, Buzsáki G. 2009. Theta Oscillations Provide Temporal
1072 Windows for Local Circuit Computation in the Entorhinal-Hippocampal Loop. Neuron.
1073 64:267–280.
1074 Mizuseki K, Sirota A, Pastalkova E, Diba K, Buzsaki G. 2013. Multiple single unit recordings
1075 from different rat hippocampal and entorhinal regions while the animals were
1076 performing multiple behavioral tasks. CRCNS.org.
1077 Mongillo G, Barak O, Tsodyks M. 2008. Synaptic theory of working memory. Science (80-).
1078 319:1543–1546.
1079 Muñoz W, Tremblay R, Levenstein D, Rudy B. 2017. Layer-specific modulation of neocortical
1080 dendritic inhibition during active wakefulness. Science (80-). 355:954–959.
1081 Murray AJ, Sauer J, Riedel G, McClure C, Ansel L, Cheyne L, Bartos M, Wisden W, Wulff P.
1082 2011. Parvalbumin-positive CA1 interneurons are required for spatial working but not
1083 for reference memory. Nat Neurosci. 14:297–299.
1084 Murray JD, Bernacchia A, Roy NA, Constantinidis C, Romo R, Wang X-J. 2017. Stable
1085 population coding for working memory coexists with heterogeneous neural dynamics in
1086 prefrontal cortex. Proc Natl Acad Sci. 114:394–399.

1087 Newman EL, Gupta K, Climer JR, Monaghan CK, Hasselmo ME. 2012. Cholinergic modulation
1088 of cognitive processing: Insights drawn from computational models. Front Behav
1089 Neurosci. 6:1–19.
1090 O'Keefe J, Dostrovsky J. 1971. The hippocampus as a spatial map. Preliminary evidence from
1091 unit activity in the freely-moving rat. Brain Res. 34:171–175.
1092 Okada K, Nishizawa K, Kobayashi T, Sakata S, Kobayashi K. 2015. Distinct roles of basal
1093 forebrain cholinergic neurons in spatial and object recognition memory. Sci Rep.
1094 5:13158.
1095 Palmigiano A, Geisel T, Wolf F, Battaglia D. 2017. Flexible information routing by transient
1096 synchrony. Nat Neurosci. 20:1014–1022.
1097 Parikh V, Kozak R, Martinez V, Sarter M. 2007. Prefrontal Acetylcholine Release Controls Cue
1098 Detection on Multiple Timescales. Neuron. 56:141–154.
1099 Pastalkova E, Itskov V, Amarasingham A, Buzsaki G. 2008. Internally Generated Cell Assembly
1100 Sequences in the Rat Hippocampus. Science (80-). 321:1322–1327.
1101 Pfeiffer BE, Foster DJ. 2013. Hippocampal place-cell sequences depict future paths to
1102 remembered goals. Nature. 497:74–79.
1103 Pi H-J, Hangya B, Kvitsiani D, Sanders JI, Huang ZJ, Kepecs A. 2013. Cortical interneurons that
1104 specialize in disinhibitory control. Nature. 503:521–524.
1105 Pinto L, Goard MJ, Estandian D, Xu M, Kwan AC, Lee S, Harrison TC, Feng G, Dan Y. 2013. Fast
1106 modulation of visual perception by basal forebrain cholinergic neurons. Nat Neurosci.
1107 16:1857–1863.
1108 Preston AR, Eichenbaum H. 2013. Interplay of hippocampus and prefrontal cortex in
1109 memory. Curr Biol. 23:764–773.

1110 Rahman J, Berger T. 2011. Persistent activity in layer 5 pyramidal neurons following
1111 cholinergic activation of mouse primary cortices. Eur J Neurosci. 34:22–30.
1112 Robinson NTM, Priestley JB, Rueckemann JW, Garcia AD, Smeglin VA, Marino FA,
1113 Eichenbaum H. 2017. Medial Entorhinal Cortex Selectively Supports Temporal Coding by
1114 Hippocampal Neurons. Neuron. 94:677-688.e6.
1115 Rotstein HG, Oppermann T, White JA, Kopell NJ. 2006. The dynamic structure underlying
1116 subthreshold oscillatory activity and the onset of spikes in a model of medial entorhinal
1117 cortex stellate cells. J Comput Neurosci. 21:271–292.
1118 Royer S, Zemelman B V, Losonczy A, Kim J, Chance F, Magee JC, Buzsáki G. 2012. Control of
1119 timing, rate and bursts of hippocampal place cells by dendritic and somatic inhibition.
1120 Nat Neurosci. 15:769–775.
1121 Sabec MH, Wonnacott S, Warburton EC, Bashir ZI. 2018. Nicotinic Acetylcholine Receptors
1122 Control Encoding and Retrieval of Associative Recognition Memory through Plasticity in
1123 the Medial Prefrontal Cortex. Cell Rep. 22:3409–3415.
1124 Schlesiger MI, Cannova CC, Boublil BL, Hales JB, Mankin EA, Brandon MP, Leutgeb JK, Leibold
1125 C, Leutgeb S. 2015. The medial entorhinal cortex is necessary for temporal organization
1126 of hippocampal neuronal activity. Nat Neurosci. 18.
1127 Spellman TJ, Rigotti M, Ahmari SE, Fusi S, Gogos JA, Gordon JA. 2015. Hippocampal–
1128 prefrontal input supports spatial encoding in working memory. Nature. 522:309–314.
1129 Stokes MG. 2015. 'Activity-silent' working memory in prefrontal cortex: a dynamic coding
1130 framework. Trends Cogn Sci. 19:394–405.
1131 Suh J, Rivest AJ, Nakashiba T, Tominaga T, Tonegawa S. 2011. Entorhinal Cortex Layer III
1132 Input to the Hippocampus Is Crucial for Temporal Association Memory. Science (80-).
1133 334:1415–1420.

1134 Swanson LW, Cowan WM. 1977. An Autoradiographic Study of the Organization of the
1135 Efferent Connections of the Hippocampal Formation in the Rat. J Comp Neurol. 172:49–
1136 84.
1137 Takahashi H, Magee JC. 2009. Pathway Interactions and Synaptic Plasticity in the Dendritic
1138 Tuft Regions of CA1 Pyramidal Neurons. Neuron. 62:102–111.
1139 Teles-Grilo Ruivo LM, Baker KL, Conway MW, Kinsley PJ, Gilmour G, Phillips KG, Isaac JTR,
1140 Lowry JP, Mellor JR. 2017. Coordinated Acetylcholine Release in Prefrontal Cortex and
1141 Hippocampus Is Associated with Arousal and Reward on Distinct Timescales. Cell Rep.
1142 18:905–917.
1143 Unal G, Joshi A, Viney TJ, Kis V, Somogyi P. 2015. Synaptic Targets of Medial Septal
1144 Projections in the Hippocampus and Extrahippocampal Cortices of the Mouse. J
1145 Neurosci. 35:15812–15826.
1146 van Strien NM, Cappaert NLM, Witter MP. 2009. The anatomy of memory: an interactive
1147 overview of the parahippocampal–hippocampal network. Nat Rev Neurosci. 10:272–
1148 282.
1149 Vogels TP, Abbott LF. 2005. Signal propagation and logic gating in networks of integrate-and-
1150 fire neurons. J Neurosci. 25:10786–10795.
1151 Vogels TP, Abbott LF. 2009. Gating multiple signals through detailed balance of excitation
1152 and inhibition in spiking networks. Nat Neurosci. 12:483–491.
1153 Wang X-J, Buzsáki G. 1996. Gamma oscillation by synaptic inhibition in a hippocampal
1154 interneuronal network model. J Neurosci. 16:6402–6413.
1155 Witter MP, Wouterlood FG, Naber PA, Van Haeften T. 2000. Anatomical organization of the
1156 parahippocampal-hippocampal network. Ann N Y Acad Sci. 911:1–24.

1157 Wolff MJ, Jochim J, Akyürek EG, Stokes MG. 2017. Dynamic hidden states underlying
1158 working-memory-guided behavior. Nat Neurosci. 20:864–871.
1159 Womelsdorf T, Valiante T a, Sahin NT, Miller KJ, Tiesinga PH. 2014. Dynamic circuit motifs
1160 underlying rhythmic gain control, gating and integration. Nat Neurosci. 17:1031–1039.
1161 Wulff P, Ponomarenko A a, Bartos M, Korotkova TM, Fuchs EC, Bähner F, Both M, Tort ABL,
1162 Kopell NJ, Wisden W, Monyer H. 2009. Hippocampal theta rhythm and its coupling with
1163 gamma oscillations require fast inhibition onto parvalbumin-positive interneurons. Proc
1164 Natl Acad Sci U S A. 106:3561–3566.
1165 Yamamoto J, Suh J, Takeuchi D, Tonegawa S. 2014. Successful Execution of Working Memory
1166 Linked to Synchronized High-Frequency Gamma Oscillations. Cell. 157:845–857.
1167 Yang GR, Murray JD, Wang X. 2016. A dendritic disinhibitory circuit mechanism for pathway-
1168 specific gating. Nat Commun. 7:12815.
1169 Zhang H, Lin S, Nicolelis MAL. 2010. Spatiotemporal coupling between hippocampal
1170 acetylcholine release and theta oscillations in vivo. J Neurosci. 30:13431–13440.
1171 Zhang S, Xu M, Kamigaki T, Hoang Do JP, Chang W-C, Jenvay S, Miyamichi K, Luo L, Dan Y.
1172 2014. Long-range and local circuits for top-down modulation of visual cortex
1173 processing. Science (80-). 345:660–665.
1174 Zheng C, Bieri KW, Hsiao YT, Colgin LL. 2016. Spatial Sequence Coding Differs during Slow
1175 and Fast Gamma Rhythms in the Hippocampus. Neuron. 89:398–408.
1176
1177